3-1-2016

X-Ray, UV And Optical Analysis Of Supergiants: ϵ Ori

R. E. Puebla

D. J. Hillier

J. Zsargó

David H. Cohen
Swarthmore College, dcohen1@swarthmore.edu

M. A. Leutenegger

Monthly Notices
of the
ROYAL ASTRONOMICAL SOCIETY
MNRAS **456,** 2907–2936 (2016) doi:10.1093/mnras/stv2783

X-ray, UV and optical analysis of supergiants: ϵ Ori

Raul E. Puebla,[1]★ D. John Hillier,[1] Janos Zsargó,[2] David H. Cohen[3] and Maurice A. Leutenegger[4,5]†‡§¶

[1]*Department of Physics and Astronomy & Pittsburgh Particle Physics, Astrophysics, and Cosmology Center (PITT PACC), University of Pittsburgh, 3941 O'Hara Street, Pittsburgh, PA 15260, USA*
[2]*Escuela Superior de Física y Matemática. Instituo Politécnico Nacional. Av. Instituto Politécnico Nacional, Edificio 9, C.P. 07738, México, DF. México*
[3]*Department of Physics and Astronomy, Swarthmore College, 500 College Ave. Swarthmore, PA 19081, USA*
[4]*CRESST/University of Maryland, Baltimore County, 1000 Hilltop Circle, Baltimore, MD 21250, USA*
[5]*NASA/Goddard Space Flight Center, 8800 Greenbelt Road, Greenbelt, MD 20771, USA*

Accepted 2015 November 24. Received 2015 November 12; in original form 2015 July 23

ABSTRACT

We present a multi-wavelength (X-ray to optical) analysis, based on non-local thermodynamic equilibrium photospheric+wind models, of the B0 Ia-supergiant: ϵ Ori. The aim is to test the consistency of physical parameters, such as the mass-loss rate and CNO abundances, derived from different spectral bands. The derived mass-loss rate is $\dot{M}/\sqrt{f_\infty} \sim 1.6 \times 10^{-6}$ M$_\odot$ yr^{-1} where f_∞ is the volume filling factor. However, the S IV $\lambda\lambda$1062,1073 profiles are too strong in the models; to fit the observed profiles it is necessary to use f_∞ <0.01. This value is a factor of 5 to 10 lower than inferred from other diagnostics, and implies $\dot{M} \lesssim 1 \times 10^{-7}$ M$_\odot$ yr^{-1}. The discrepancy could be related to porosity–vorosity effects or a problem with the ionization of sulphur in the wind. To fit the UV profiles of N V and O VI it was necessary to include emission from an interclump medium with a density contrast ($\rho_{\rm cl}/\rho_{\rm ICM}$) of ∼100. X-ray emission in H/He like and Fe L lines was modelled using four plasma components located within the wind. We derive plasma temperatures from 1×10^6 to 7×10^6 K, with lower temperatures starting in the outer regions ($R_0 \sim$ 3–6 R$_*$), and a hot component starting closer to the star ($R_0 \lesssim 2.9$ R$_*$). From X-ray line profiles we infer $\dot{M} < 4.9 \times 10^{-7}$ M$_\odot$ yr^{-1}. The X-ray spectrum (≥0.1 kev) yields an X-ray luminosity $L_{\rm X} \sim 2.0 \times 10^{-7} L_{\rm bol}$, consistent with the superion line profiles. X-ray abundances are in agreement with those derived from the UV and optical analysis: ϵ Ori is slightly enhanced in nitrogen and depleted in carbon and oxygen, evidence for CNO processed material.

Key words: techniques: spectroscopic – stars: abundances – stars: individual: ϵ Ori – stars: massive – stars: mass-loss – supergiants.

1 INTRODUCTION

Massive stars play a fundamental role in the Universe. Considered the progenitors of core collapse supernovae, they are also responsible for galactic H II regions, the transfer of mass, momentum and energy to the interstellar medium (ISM), and for metal enrichment in their host galaxy.

Among stellar wind properties, the mass-loss rate ($\dot{M}$) is crucial for understanding the evolution of massive stars. $\dot{M}$ affects the star's lifetime on the main sequence, the rotation rate of the star, and the star's subsequent evolution (e.g. Chiosi & Maeder 1986; Maeder & Meynet 2000). The first estimates for $\dot{M}$ were derived assuming spherical smooth winds. However, subsequent observations reveal inconsistencies. For instance, the far-UV resonance line profiles (e.g. P V and S IV) observed by *Copernicus* and *FUSE* cannot be simultaneously fitted with Hα (e.g. Crowther et al. 2002; Hillier

★E-mail: rep54@pitt.edu

†Based on observations obtained with *XMM–Newton*, an ESA science mission with instruments, contributions directly funded by ESA Member States, NASA.

‡The scientific results reported in this article are based on data obtained from the Chandra Data Archive.

§Some of the data presented in this paper were obtained from the Mikulski Archive for Space Telescopes (MAST). STScI is operated by the Association of Universities for Research in Astronomy, Inc., under NASA contract NAS5-26555. Support for MAST for non-*HST* data is provided by the NASA Office of Space Science via grant NNX09AF08G, by other grants, contracts.

¶Optical data for this work were obtained from *POLARBASE* (Petit et al. 2014).

2003). Furthermore, P Cygni profiles from highly ionized species, such as N V and O VI, were detected in the UV spectrum (Snow & Morton 1976), but such ionization states are incompatible with radiative equilibrium in a smooth wind. Cassinelli & Olson (1979) suggested that these ions could be produced by Auger ionization by X-rays (double ionization due to ejection of an inner shell electron by an X-ray photon), a suggestion confirmed by *Einstein* X-ray Observatory which found that massive stars are strong X-ray sources (Harnden et al. 1979; Seward et al. 1979). Two scenarios were proposed to explain the observed X-ray emission: emission from a corona just above the photosphere (Hearn 1975; Cassinelli & Olson 1979) and X-ray emission from shock-heated plasma distributed throughout the wind (Lucy & White 1980; Lucy 1982; Owocki, Castor & Rybicki 1988). The latter is now generally accepted as the dominant X-ray emission mechanism in single stars.

Because of the deficiencies discussed above, the 'standard' smooth wind model needed to be revised. At present, it is widely accepted that the winds of massive stars are strongly structured (clumped). The existence of such winds is supported by hydrodynamical time-dependent simulations that predict that radiation-driven winds are unstable (Owocki et al. 1988; Feldmeier, Puls & Pauldrach 1997; Runacres & Owocki 2002). Evidence for these inhomogeneities has been found, for instance, by observations of variable discrete absorption components (DAC) in UV and optical lines (e.g. Fullerton, Gies & Bolton 1996; Kaper et al. 1996; Morel et al. 2004; Prinja et al. 2006), and from observations of stochastic variability (e.g. Eversberg, Lépine & Moffat 1998). Hillier (1991) showed that the electron scattering wings of recombination lines of Wolf–Rayet (WR) stars cannot be reproduced by smooth winds, necessitating clumped models and lower mass-loss rates to fit them.

Clumping can be treated using two approximations. The simplest approach considers optically thin clumps at all wavelengths ('*microclumping*'). The second approach allows for the optical thickness of clumps, especially for lines ('*macroclumping*'). Commonly it is assumed that the interclump medium is void. However, recently it has been shown that its influence is not negligible (e.g. Zsargó et al. 2008).

Microclumping has been used to lower the discrepancy between P V UV resonance lines and Hα. Typical filling factors in O stars are 0.01 to 0.1, although, in some cases, it still may be necessary to reduce the P abundance by a factor of 2 from the expected value (e.g. Crowther et al. 2002; Hillier 2003; Bouret, Lanz & Hillier 2005; Fullerton, Massa & Prinja 2006; Bouret et al. 2012). The principal consequence of microclumping is a reduction of mass-loss rates by factors from 3 to 10.

A 3D Monte Carlo simulation performed by Šurlan et al. (2013) showed that when macroclumping is included the Hα and P V lines discrepancy is fixed for higher values of the volume filling factor, yielding higher mass-loss rates when compared with those based on pure microclumping (see also Oskinova, Hamann & Feldmeier 2007; Sundqvist, Puls & Feldmeier 2010; Šurlan et al. 2012).

The problem with all these analyses is degeneracy – there are several parameters which can be varied but only a few lines that can be modelled, making it difficult to reach definitive conclusions (see details in Šurlan et al. 2013).

As noted by several authors (e.g. Cohen et al. 2010), the fitting of X-ray lines provides an independent method to estimate the mass-loss rates of OB stars. Cohen et al. (2010) estimated the characteristic optical depth for X-rays ($\tau_* = \kappa \dot{M}/4\pi R_* v_\infty$), fitting separately X-ray lines and then fitting the best optical depth wavelength distribution using the mass-loss rate as a free parameter. The main reported problem with X-ray line emission is that most of the observed profiles are fairly symmetric. This contradicts models that predict lines skewed to the blue (Macfarlane et al. 1991; Owocki & Cohen 2001). Three explanations are currently proposed: resonance scattering, lower mass-loss rates and porosity [see Oskinova et al. (2011) for a summary of X-ray emission properties of OB stars]. However, resonance scattering cannot explain all observed line profiles (Ignace & Gayley 2002; Leutenegger et al. 2007), while the needed reduction in the mass-loss rates inferred from Hα is large (factors of 2 to 10) (e.g. Cohen et al. 2014a). It has also been argued that the porosity lengths (a measure of the mean-free path of photons between clumps) required to get symmetric lines are unlikely to be as large as needed (Owocki & Cohen 2006). Sundqvist et al. (2012) and Leutenegger et al. (2013) concluded that a porosity consistent with the observed X-ray line profiles cannot affect the mass-loss rate determination significantly. Furthermore, Hervé, Rauw & Nazé (2013) showed that porosity is not important to explain the X-ray spectrum of ζ Pup.

With the aim of providing more rigorous constraints, and reducing systematic errors, we present our work on a multi-wavelength analysis of the supergiant ϵ Ori. The analysis is based on X-ray data from *Chandra* and *XMM–Newton*, UV data from *IUE*, *HST*, and the *Copernicus* satellite, and optical data taken from the *POLARBASE* archive. The photospheric, wind and hot-plasma parameters are obtained from a modified version of CMFGEN (Hillier & Miller 1998), and the consistency of the derived parameters is examined.

The paper is constructed as follows. In the next section, we present results from previous analyses of ϵ Ori and its main spectral features. Observational data are described in Section 3 while the method and model assumptions are presented in Section 4. The results of optical, UV and X-ray analysis are given in Section 5. A discussion of the results and conclusions are provided in Sections 6 and 7.

2 ϵ ORI (HD 37128)

The B0 Ia supergiant star ϵ Ori (HD 37128) is the central star of the Orion Belt, and is also known as *Alnilam* [an Arabic word that means '*string of pearls*' (Knobel 1909)] and belongs to the Orion OB1(b1) association.

The first attempts to derive the physical parameters for ϵ Ori using photospheric models in non-local thermodynamic equilibrium (NLTE) were made by Auer & Mihalas (1972) and Lamers (1974) who used optical line profiles, and found an effective temperature around 29 000 K and $\log g = 3.0$. McErlean, Lennon & Dufton (1998) using an NLTE model found similar parameters, while Kudritzki et al. (1999), using the original version of the code FASTWIND (Santolaya-Rey, Puls & Herrero 1997; Puls et al. 2005), found $T_{\rm eff} = 28\,000$ K and $\log g = 3.0$.

Crowther, Lennon & Walborn (2006) and Searle et al. (2008) used the NLTE transfer code CMFGEN (Hillier & Miller 1998) to derive effective temperatures of 27 000 K and 27 500 K, respectively. However, there exists a discrepancy between their $\log g$ values – Crowther et al. reported a value of 2.9 while Searle et al. reported 3.1. Both works also analysed the CNO abundances of ϵ Ori. In contrast to the nitrogen deficiency reported by Walborn (1976), Crowther et al. reported a slight enrichment of nitrogen and depletion of carbon. On the other hand, Searle et al. found a nitrogen and carbon deficiency and a solar oxygen abundance.

Previous values for mass-loss rate from different diagnostics encompass values from 1.5×10^{-6} to 4.3×10^{-6} $M_\odot\,yr^{-1}$. Diagnostics include Hα strength (Kudritzki et al. 1999; Urbaneja 2004; Crowther et al. 2006; Searle et al. 2008), UV P Cyg profiles (Howarth & Lamers 1999), thermal radio fluxes (Lamers &

Leitherer 1993; Blomme et al. 2002) as well as H and He infrared lines in the *H* and *K* bands (Repolust et al. 2005; they derived an upper limit of $\dot{M} = 5.25 \times 10^{-6}$ M$_\odot$ yr^{-1}). These values were derived using smooth winds. In a subsequent analysis by Najarro, Hanson & Puls (2011), lines from the *L* band were used in conjunction with UV and optical data to obtain a mass-loss rate of $\dot{M}/\sqrt{f_\infty} = 2.65 \times 10^{-6}$ M$_\odot$ yr^{-1} and a filling factor $f_\infty = 0.03$.

Mass-loss rate determinations should all be scaled to the same distance, since the mass-loss rate typically scales as $d^{1.5}$ for ρ^2 dependent diagnostics (or d for ρ dependent diagnostics such as X-ray profiles). Distance estimates for ϵ Ori tend to cluster around 400 pc (Lesh 1968; Lamers 1974; Savage et al. 1977; Brown, de Geus & de Zeeuw 1994), and are broadly consistent with the initial *Hipparcos* determination of 412 pc (Perryman et al. 1997). However, with the latest calibration the new estimate is 606 pc (van Leeuwen 2007). This distance is the highest ever estimated, and substantially increases the luminosity and mass-loss rate for ϵ Ori.

IUE and *Copernicus* spectra of ϵ Ori show line emission from N V and O VI resonance transitions, which, given the effective temperature of ϵ Ori, provides evidence of X-ray emission in the wind. *Chandra* and *XMM* spectra of HD 37128 show strong emission lines from H/He-like atoms of C, N, O, Ne, Mg and Si as well as Fe XVII lines.

Previous analyses of X-ray emission from ϵ Ori found a wide spatial distribution of the hot plasma in the wind. Cohen et al. (2014a) fitted *Chandra* lines and did not find any correlation between the onset radius for emitting plasma and the emitting ion. This confirmed the results by Leutenegger et al. (2006) who found no evidence for different spatial distributions for different ions.

Recently, Cohen et al. (2014a) estimated the mass-loss rate for ϵ Ori by fitting X-ray line profiles. They reported two values of mass-loss rate: 2.1×10^{-7} M$_\odot$ yr^{-1} and 6.5×10^{-7} M$_\odot$ yr^{-1}. The first value uses nine X-ray lines while the second value excludes three lines that might be influenced by resonance scattering.

ϵ Ori shows spectral variability in both the optical and UV. The main variability detected in the UV is associated with DACs, especially in the blue wing of the Si IV and N V doublets. Some other UV lines, including string photospheric lines, also show variability (Prinja, Massa & Fullerton 2002). In the optical Hα shows strong variability with changes in both shape and strength occurring on a time-scales of hours to tens of days (e.g. Ebbets 1982; Morel et al. 2004; Prinja et al. 2004; Thompson & Morrison 2013, and references therein). One possible cause of the variability is radial and non-radial oscillations that produce a mass-loss rate modulation (Thompson & Morrison 2013). Our calculations show that variations of ±30 per cent in $\dot{M}$ about our derived value can explain the observed variations of Hα.

We chose ϵ Ori as a standard early B-supergiant due to the availability of high-resolution X-ray, UV and optical data. In practice, spectral variability is common is B-supergiants, and hence unavoidable. Its variability will introduce uncertainties in the derived wind parameters, but these uncertainties can be qualified, and will not affect our main aim of evaluating the consistency of the main physical parameters of ϵ Ori derived in this multi-wavelength analysis.

3 THE DATA

For this work we collected optical, UV and X-ray data from different archives as described below. The sources of the data are presented in Table 1.

3.1 Optical data

The optical data were obtained from *POLARBASE*,[1] the stellar spectra archive for the *NARVAL* and *ESPaDOns* echelle spectropolarimeters. The former is installed in the Télescope Bernard Lyot (TBL; Pic du Midi Observatory) and the latter at the Canada–French–Hawaii Telescope. A detailed description of these instruments can be found in Silvester et al. (2012) and Petit et al. (2014). They are twin spectropolarimeters except for the aperture (2.8 arcsec for *NARVAL* and 1.6 arcsec for *ESPaDOns*). Both of them have a spectral resolution $R = \lambda/\Delta\lambda \simeq 65\,000$ and a spectral coverage from 3690 to 10 000 Å. The wavelength calibration is performed using a Th-Ar spectra and it is refined using telluric bands as references for radial velocity. The instruments have two modes of operation: spectroscopic and polarimetric. In the polarimetric mode, the beam is split with a Wolloston prism, and the new beams are then conducted to a spectrometer through fibres. The *I* Stokes parameter is obtained by adding these two spectra; the rest of the Stokes parameters (*V*, *Q* and *U*) are extracted by combinations as described by Bagnulo et al. (2009)(see also Petit et al. 2014).

The early B-supergiant star ϵ Ori has been observed by both of these instruments at different epochs. Because of its spectral variability we selected for this work one set of 112 exposures taken by *NARVAL* on 2007 October 19 during 4 h (universal time from archive) in polarimetric mode. Every exposure has a signal-to-noise ratio of $\sim$ 600. The reduction for each of these exposures was automatically performed by the Libre-Esprit reduction pipeline (Petit et al. 2014). We chose the '*I*' Stokes spectra from the archive for this work. All of the exposures were combined and the resulting spectrum normalized using soft spline functions between nodes chosen by visual exploration to avoid spurious oscillations. This task was performed with the `line_norm` procedure from FUSE IDL tools.[2] This combined and normalized spectrum was used for the analysis.

3.2 UV data

3.2.1 IUE

The *International Ultraviolet Explorer* (*IUE*) has observed ϵ Ori in both low- and high-dispersion modes. For this work, we selected data obtained for the BSIGP program (PI: Geraldine Peters) from the MAST[3] archive. These 10 exposures of ϵ Ori were undertaken from 1987 January 28 to 1987 February 6 in high dispersion and utilizing the large aperture with the short-wavelength prime camera (SWP). This instrument configuration yields a spectral resolution of $\lambda/\Delta\lambda$ $\sim$10 000 with a spectral coverage of $\lambda\lambda$1150–1975. When extracted, the spectra did not show strong variability, so we combined them to obtain the final mean spectrum.

The *IUE* observation program HSCAD (PI: A.K. Dupree) has 33 exposures of ϵ Ori taken through the small aperture. When combined and scaled to BSIGP fluxes, no significant differences were detected when compared with the higher signal-to-noise ratio BSIGP observations.

For long wavelengths we averaged the three exposures made on 1979 January 9 using the Long-Wavelength Redundant (LWR) camera (1900–3080Å) at high dispersion ($\lambda/\Delta\lambda \sim$ 14 000) and small aperture. This data were collected within the program ID: UK022 (PI: P. Byrne).

[1] http://polarbase.irap.omp.eu/
[2] http://fuse.pha.jhu.edu/analysis/fuse_idl_tools.html
[3] http://archive.stsci.edu/

Table 1. Summary of data of ϵ Ori: optical (*NARVAL*), ultraviolet (*IUE*, *HST* and *Copernicus*) and X-ray (*Chandra* and *XMM–Newton*).

ID Obs.	Date	Julian date	Spectral range (Å)	$\lambda/\Delta\lambda$
		NARVAL (Optical)		
–	Oct-19-2007	245 4392.55907	3690–10000	65 000
		IUE (UV)		
SWP30177	Jan-28-1987	244 6823.57668	1150–1975	10 000
SWP30196	Jan-30-1987	244 6825.56254	1150–1975	10 000
SWP30204	Jan-31-1987	244 6826.54533	1150–1975	10 000
SWP30216	Feb-01-1987	244 6827.57926	1150–1975	10 000
SWP30225	Feb-01-1987	244 6828.47190	1150–1975	10 000
SWP30242	Feb-03-1987	244 6829.64887	1150–1975	10 000
SWP30249	Feb-03-1987	244 6830.47746	1150–1975	10 000
SWP30257	Feb-05-1987	244 6831.64990	1150–1975	10 000
SWP30266	Feb-06-1987	244 6832.66278	1150–1975	10 000
SWP30272	Feb-06-1987	244 6833.47835	1150–1975	10 000
LWR02238	Sept-01-1978	244 3753.35590	1900–3080	14 000
LWR02239	Sept-01-1978	244 3753.40463	1900–3080	14 000
LWR02240	Sept-01-1978	244 3753.42454	1900–3080	14 000
		GHRS (UV)		
Z1BW040TT	Nov-11-1994	2449302.5975	1180–1218	20 000
Z1BW040UT	Nov-11-1994	2449302.5000	1229–1268	20 000
Z1BW040VT	Nov-11-1994	2449302.5019	1273–1311	20 000
Z1BW040WT	Nov-11-1994	2449302.5389	1324–1363	20 000
Z1BW040XT	Nov-11-1994	2449302.5408	1385–1423	20 000
Z1BW040YT	Nov-11-1994	2449302.5428	1527–1564	20 000
Z1BW040ZT	Nov-11-1994	2449302.5634	1588–1625	20 000
Z1BW0400T	Nov-11-1994	2449302.5656	1649–1684	20 000
		Copernicus (UV)		
027	Nov-30-1972	244 1652.49738	1000–1420	5500
		Chandra (X-ray)		
3753	Dec-12-2003	245 2986.00475	2–26	150–1100
		XMM–Newton (X-ray)		
0112400101	Mar-06-2002	245 2339.84921	5–35	150–800

3.2.2 *GHRS*/HST

Hubble Space Telescope (*HST*) observed ϵ Ori only with the Goddard High Resolution Spectrograph (*GHRS*) (programs: 3472, 60706541, 3859 and 6249). As the programs focused on interstellar abundances using specific diagnostic lines, none of the observations covered a wide spectral range. We used the observations from program 3472 (PI: Lewis Hobbs), which were collected on 1994 November 11. We retrieved the calibrated data from the G160M first-order grating at intermediate resolution ($R \simeq 25\,000$) from the MAST archive. We treated the data using the STSDAS package and related tasks from analysis software IRAF.[4]

3.2.3 *Copernicus*

Copernicus observations of ϵ Ori (star: 027) were also retrieved from the MAST archive. We selected scans that covered a large spectral range, and that included O VI λ1032,1038, S IV λ1062,1073 and P V λ1118,1028. We co-added those scans and generated the spectrum using the IDL IUEDAC[5] library tools and normalized it using soft spline functions between selected nodes in the same sense as explained above for the optical data. After selecting, co-adding and normalizing, we obtained a spectrum with coverage of $\lambda\lambda$1000–1450.

3.3 X-ray data

3.3.1 *Chandra*

Chandra observed ϵ Ori on 2003 December 12, using the gratings of HETGS (High Energy Transition Grating Spectrometer) for 92 ks (PI: Wayne Waldron). The full width at half-maximum spectral resolutions are 23 and 12 mÅ for Medium Energy Grating (MEG) and High Energy Grating (HEG), respectively. The effective area of these gratings is significant for $\lambda \gtrsim 2$ Å but falls strongly beyond $\lambda \gtrsim 16$ Å in the case of HEG and $\lambda \gtrsim 25$ Å for MEG. Because of the small number of counts collected in the HEG, we only used MEG data for this work. We reprocessed the data using the CIAO version 4.6 tasks, following the standard threads as described in the CIAO documentation. We combined the positive and negative first-order MEG spectra using ADD_GRATING_ORDERS task.

3.3.2 *XMM–Newton*

XMM–Newton observed ϵ Ori on 2002 March 6 using the instruments: EPIC-MOS(1,2), EPIC-pn and the Reflection Grating

[4] http://iraf.noao.edu/
[5] http://archive.stsci.edu/iue/iuedac.html

Table 2. Species and ions included in CMFGEN models. F is the number of levels for each atomic model and S denotes the super-levels used in calculations. 'E\I' denotes Element\Ionization.

E\I	I		II		III		IV		V		VI		VII	
	F	S	F	S	F	S	F	S	F	S	F	S	F	S
H	30	20												
He	69	45	30	22										
C			92	40	84	51	64	64						
N			85	45	82	41	76	44	49	41				
O			123	54	170	88	78	38	56	32				
Ne					71	28	52	17	166	37				
Si			100	72	33	33	33	22						
P							90	30	62	16				
S					44	24	142	51	98	31				
Fe					1433	104	520	74	220	50	433	44	153	29

Spectrometers (RGS1 and RGS2) (PI: Martin Turner). Our analysis was based only on the RGS data due to its high spectral resolution ($R \sim 250$ at 15 Å). The exposure time for both spectrometers was 13 ks.

The data were reduced following standard procedures with SAS v13.5.0. We use the first-order spectra of each spectrometer (RGS1 and RGS2) for the analysis. Together, RGS1 and RGS2 have a spectral coverage from 6 to 39 Å.

4 THE METHOD

The analysis was undertaken in two main stages. In the first stage we derived the photospheric and wind parameters using the standard method for massive stars and the latest version of CMFGEN. In the second stage, the X-ray emission is modelled. We then tested the consistency of the adopted parameters with the X-ray line profiles (mass-loss rates) and line ratios (abundances).

4.1 Modelling assumptions

4.1.1 Optical and UV analysis

The calculations for our analysis were performed using the code CMFGEN (Hillier & Miller 1998). This code models a spherical stellar atmosphere and stellar wind solving the radiative transfer, radiative and statistical equilibrium equation system in non-LTE (NLTE) taking into account line-blanketing effects. The transfer equation is solved in the comoving frame (CMF). Table 2 describes the ionization states and number of full atomic levels and super-levels for each atomic species included in the models.

The photospheric density structure is calculated by iteratively solving the hydrostatic equilibrium equation system below the sonic point as described by Bouret et al. (2012). Given an adopted mass-loss rate and the velocity profile $v(r)$, the wind density structure is calculated using the continuity equation. The adopted velocity profile is similar to that commonly used for massive star winds (e.g. Hillier 2003):

$$v(r) = \frac{2v_{\rm tr} + (v_\infty - 2v_{\rm tr})(1 - r_{\rm tr}/r)^\beta}{1 + \exp\left[(r_{\rm tr} - r)/h_{\rm eff}\right]}, \quad (1)$$

where $v_{\rm tr}$ and $r_{\rm tr}$ are the transition velocity and radius, between the photosphere and wind. The transition point is set as the radius where $v(r_{\rm tr}) = 0.75 v_{\rm s}$ where $v_{\rm s} \sim 15$ km s^{-1} is the sound velocity. The term $h_{\rm eff} = v_{\rm tr}/(2({\rm d}v/{\rm d}r)_{\rm tr})$ is the scale height, v_∞ is the terminal velocity and β is the acceleration parameter.

Clumping is taken into account through the volume filling factor $f = \bar{\rho}/\rho(r)$, where $\bar{\rho}$ is the homogeneous (unclumped) wind density and ρ is the density in clumps. In this approach the clumps are assumed to be optically thin to radiation and the interclump medium is void (Hillier & Miller 1999). The filling factor dependence with radius is defined by the relation: $f = f_\infty + (1 - f_\infty)\exp(-v(r)/v_{\rm cl})$, where $v_{\rm cl}$ characterizes the velocity where clumping starts.

It is well known that we need to include the effect of microturbulence on the photospheric and wind spectrum (e.g. Howarth et al. 1997). For the formal solution, the depth dependence of the microturbulence velocity was parametrized as in Hillier (2003): $\xi_t = \xi_{\rm min} + (\xi_{\rm max} - \xi_{\rm min})v(r)/v_\infty$. Here, $\xi_{\rm min}$ and $\xi_{\rm max}$ are the photospheric and wind turbulence, respectively. In this work we varied the $\xi_{\rm min}$ from 10 to 20 km s^{-1}, a reasonable range for early B-supergiant stars (McErlean et al. 1998) and $\xi_{\rm max} \sim 0.1$–$0.3\ v_\infty$. In the CMFGEN calculation we used a microturbulent velocity that was independent of depth.

4.1.2 X-ray analysis

We assume that the X-ray emission comes from an ensemble of shock-heated regions within the wind (shock scenario). The shock scenario predicts regions distributed in the wind where the plasma is strongly heated due to shocks caused by radiative instabilities (Owocki et al. 1988; Feldmeier et al. 1997).

The current version of CMFGEN allows for X-ray emission from shocked regions in the wind using emissivity tables from APEC (Smith et al. 2001) for different temperatures, but it does not take into account differences in abundances (generally), densities or the influence of the UV radiation on the populations of the levels that give rise to the X-ray lines.

Recently, Zsargó et al. (in preparation) developed a new version called XCMFGEN that makes possible a consistent interaction between the code APEC and CMFGEN. Here we will briefly describe the main features of the method to compute the synthetic X-ray spectrum taking into account the wind radiation from CMFGEN.

As a convenient approximation, a set of $N_{\rm p}$ plasmas, characterized by their temperature ($T_{\rm X}$), the radius where the plasma emission starts (R_0), and the X-ray filling factor ($f_{\rm X}$), are distributed within the wind. The filling factor is parametrized as follows:

$$f_{\rm X\text{-}ray}(r) = \begin{cases} f_{\rm X} & \text{if } r \geq R_0 \\ f_{\rm X} \exp^{-(v(R_0)/v(r))^2 (R_0/r)^4} & \text{if } r < R_0, \end{cases} \quad (2)$$

where $v(r)$ is the wind velocity profile and $f_{\rm X}$ is the filling factor at infinity. An iterative process is then performed to derive the best estimates of the plasma parameters. A XCMFGEN run is done to calculate the stellar wind structure. Then, APEC is called in order to

calculate a grid of plasma emissivities covering the wind densities and plasma temperatures. The relation between the plasma and wind density is set as: $n_{\rm plasma} = 4n_{\rm wind}$ (adiabatic shock approximation). Here $n_{\rm wind}$ corresponds to the density of the unclumped model. The relation between the plasma and wind density only has a very minor influence on the analysis – its primary effect will be in the interpretation of the derived filling factors (e.g. what fraction of the wind is shocked).

The Astrophysical Plasma Emission Code (APEC) is a code for calculating level populations and emissivities for a hot plasma in collisional equilibrium. This code uses an extensive library of cross-sections (ATOMDB[6]). In this work we use this library as it is described in Foster et al. (2012). Some changes were implemented in APEC in order to read the XCMFGEN outputs as well as to use the corresponding abundances. The main change was the inclusion of the radiative excitation (i.e. UV photoexcitation) and deexcitation rates in the statistical equilibrium equations. The UV emission from the wind affects the forbidden to intercombination ratio $R = f/i$ of the He-like triplets (Gabriel & Jordan 1969; Porquet et al. 2001).

Once APEC has calculated the grid of plasma emissivities, a new run of XCMFGEN is performed including the emissivities from APEC. This process yields a new radiation field that is used in a second APEC computation. Usually, it is necessary for only two loops (i.e. XCMFGEN → APEC → XCMFGEN → APEC → XCMFGEN) to get a consistent model.

A necessary condition to apply this method is that the X-rays do not strongly affect the bulk of the cool wind. As noted previously by Martins et al. (2005) and Macfarlane, Cohen & Wang (1994), this condition holds for early O supergiants. However, for late O and B stars X-rays could change the wind ionization in a non-negligible way. An analysis of that influence in the case of ϵ Ori is presented in Section 6.3. We conclude that for clumped wind models this effect is low enough to apply this method. Thus, we applied the same fit procedure described by Zsargó et al. (in preparation) in their study of ζ Pup and did the X-ray analysis separately from the optical and UV analysis.

We created a two-dimensional grid in ($T_{\rm X}$, R_0), varying each of them between the following ranges: $T_{\rm X} = 1.0$–16.0×10^6 K and $R_0 = 1.2$–$6.1 R_*$. We then used CMF_FLUX to compute the X-ray spectrum for each ($T_{\rm X}$, R_0) combination. The starting filling factor is fixed at $f_{\rm X} = 5 \times 10^{-5}$; the corresponding value for each plasma component is adjusted subsequently as described below.

The total X-ray spectrum results from adding the contributions from each plasma component after it has propagated through the wind. We adjusted the plasma distributions (i.e. number of components, $T_{\rm X}$, R_0 and $f_{\rm X}$) using the fitting package XSPEC (Arnaud 1996) of HEASARC.[7] A multiplicative model is included to take into account the effect of interstellar absorption on the X-ray spectrum. The column density of neutral H used in this work is $\log[N({\rm H\,I})]\ {\rm cm}^{-2} = 20.48$ (Diplas & Savage 1994). As the molecular absorption in the direction of ϵ Ori is low it does not affect the X-ray spectrum and hence is ignored.

Because of the small number of counts in the *Chandra* and *XMM–Newton* observations, Poisson noise dominates, and we use the C-statistic (Cash 1979) to determine the quality of the fits. While an arbitrary number of components can be included, the final models were typically composed of only four different temperatures.

The X-ray lines included in the analyses are listed in Table 3.

Table 3. ϵ Ori *Chandra* and *XMM–Newton* lines. Data from ATOMDB.

Ion	Wavelength (Å)	Type	$T_{\rm peak}$ (10^6 K)
Si XIV	6.1822	H-like	15.8
Si XIII	6.6479, 6.6866, 6.6866	He-like	10.0
Al XII	7.7573, 7.8070, 7.8721	He-like	7.94
Mg XI	7.8503	He-like	6.31
Mg XII	8.4210	H-like	10.0
Mg XI	9.1687, 9.2297, 9.3143	He-like	6.31
Ne X	10.2388	H-like	6.31
Ne IX	11.5440	He-like	3.98
Ne X	12.1339	H-like	6.31
Fe XVII	12.2660	L-shell	6.31
Ne IX	13.4470, 13.5520, 13.6980	He-like	3.98
Fe XVII	14.2080	L-shell	7.94
Fe XVII	15.0140	L-shell	6.31
Fe XVII	15.2610	L-shell	6.31
Fe XVII	16.0040	L-shell	7.94
O VIII	16.0060	H-like	3.16
Fe XVII	16.7800	L-shell	6.31
Fe XVII	17.0510	L-shell	6.31
Fe XVII	17.0960	L-shell	6.31
O VII	18.6270	He-like	2.00
O VIII	18.9670	H-like	3.16
O VII	21.6020, 21.8040, 22.0980	He-like	2.00
N VII	24.7790	H-like	2.00
N VI	24.8980	He-like	1.59
C VI	26.9900	H-like	1.59
C VI	28.4650	H-like	1.59
N VI	28.7870, 29.0810, 29.5340	He-like	1.58
C VI	33.7370	H-like	1.26

4.2 Stellar parameters

We used the optical spectrum to estimate the photospheric parameters such as the effective temperature, gravity and surface abundances. The method follows the analysis route described by Bouret et al. (2012) (see also Martins et al. 2005; Bouret et al. 2013). We adopted a radial velocity $v_{\rm r} = 25.9 \pm 0.9$ km s^{-1} (Evans 1967).

A brief description of steps taken to derive the fundamental stellar parameters ($T_{\rm eff}$, $\log g$, and CNO, Fe and Si abundances) follows.

4.2.1 Luminosity

We adopt two distances: the distance $d = 411.5^{+245}_{-112}$ pc (Perryman et al. 1997) from the old *Hipparcos* catalogue (HIP 26311),[8] and $d = 606^{+227}_{-130}$ pc (van Leeuwen 2007) who re-calibrated *Hipparcos* data. The errors on the distance are approximately 30–50 per cent, which will yield an error on the luminosity of 60–100 per cent, and a similar, but somewhat smaller, uncertainty on the mass-loss rate.

A first estimation of luminosity was made based on M_V and the bolometric correction (BC). The last one was taken from the relation between $T_{\rm eff}$ and BC calculated by Crowther et al. (2006) (fig. 4). This relation comes from their sample of Galactic B-supergiants and from the SMC B-supergiants reported by Trundle et al. (2004) and Trundle & Lennon (2005). For this first approach we used the temperature estimated by Crowther et al. for ϵ Ori, $T_{\rm eff} = 2.7 \times 10^4$ K. The M_V value was estimated from the distance values from *Hipparcos*, the apparent visual magnitude $V = 1.69$ (Lee 1968) and the interstellar visual extinction $A_V = 3.1\ E(B-V)$, with $E(B-V)$

[6] www.atomdb.org
[7] http://heasarc.gsfc.nasa.gov/
[8] http://vizier.u-strasbg.fr/viz-bin/VizieR-2

taken from the Crowther et al. study, $E(B-V)=0.06$. Thus, $M_V=-6.57$ for $d=411.5$ pc and $M_V=-7.41$ for $d=606.06$ pc. The luminosity is given by

$$\log(L_*/L_\odot)=(M_{B\odot}-M_V-BC)/2.5, \quad (3)$$

where $M_{B\odot}$ is the solar bolometric magnitude ($M_{B\odot}=4.75$).

Once the temperature and gravity were estimated, we used the UV flux, and the optical magnitudes (*UVB*) in order to re-estimate simultaneously the luminosity and $E(B-V)$ values.

4.2.2 Gravity and effective temperature

For estimating the effective temperature and gravity ($\log g$) a small grid of models encompassing $T_{\rm eff}=2.5$–2.9×10^4 K and $\log g=2.8$ to 3.4, with steps of 0.1×10^4 K and 0.1 dex, respectively, were computed. The gravity was estimated by fitting the wings of Hβ, Hγ, Hδ and Hϵ – the lines were equally weighted for the gravity analysis. Because of the mass-loss rate of ϵ Ori, these Balmer lines are only very weakly influenced by wind emission. In order to reduce the degeneracy between $\log g$ and $T_{\rm eff}$, the equivalent widths (EWs) for He I and He II lines were also utilized. The lines used were: He I λλ4010, 4389, 5049 and He II λλ4201, 4542. These lines show a weak dependence on the microturbulence.

For computing the effective temperature, we used the ionization balance of both He I to He II and Si III to Si IV. We used the same grid described above to fit the Si IV λ4090, Si IV λ4115 and Si III λ4554–76 lines beside the He I λλ4471, 4389, 4922 and the He II lines described above. UV lines, especially those belonging to Fe IV (1550–1700 Å), Fe V (1360–1385 Å) as well as Fe III (1800–1950 Å), were used to check the result.

4.2.3 Microturbulence

To estimate the photospheric microturbulent velocity we calculated spectra for three values of $\xi_{\rm min}$ (10, 15 and 20 km s^{-1}) and fitted the EW of the 4472, 5017and 6680 Å He I lines, and the Si III triplet at 4554–4576 Å. Our exploration of synthetic spectra shows that these lines depend strongly on the $\xi_{\rm min}$ value and are weakly influenced by blending or abundance effects.

4.2.4 Surface abundances

Once the temperature and gravity were constrained, we determined the surface abundances of the main species, namely He, C, N, O, Si and Fe as follows:

Helium. As pointed out by McErlean, Lennon & Dufton (1999) and McErlean et al. (1998), it is difficult to determine the He abundance in B stars primarily because triplet and singlet lines of He I yield different He abundances. Najarro et al. (2006) showed that some He I singlets are influenced by a strong interaction of the He I resonance transition at λλ4923,5017 with UV Fe IV lines. This interaction directly affects He I 2p 1P$^{\rm o}$, which influences the strength of optical singlet lines that makes them unreliable diagnostics. Najarro et al. suggest using triplet lines for analysis. Based on these issues we decided to set the He abundance, expressed as $y=N[{\rm He}]/N[{\rm He}+{\rm H}]$, to the solar value $y=0.091$ for every one of our models.

Carbon. In the optical, we used lines of C II λλ4267,6578–82, C III λλ4070,5696,4648–50 and C IV λλ5802–12. In the case of C III λ4648 and C III λ5696, Martins & Hillier (2012) showed that these lines have strong interactions with the UV lines Fe IV λ538 and C III λ538, hence, they need be treated carefully. UV lines were used to check the abundance deduced from optical lines. We mainly used C III λ1176. The commonly used line C IV λ1169 is not detected in UV data, since it is blended with C III λ1176. The line C III λ1247 is blended with N V λ1238–42 emission and only the red emission can be used as a diagnostic.

Nitrogen. To estimate the nitrogen abundance we used the blend-free lines N II λλ3995, 4042–45, 4238–42, 5002–06, 5677–81, and N III λλ4380, 4635. As a consistency check we also examined N II λ5046 and N III λλ4098, 4512–18, 4643, 4868. The former line is blended with He I λ5049 while N III λ4098 is blended with Hδ. In the UV we used N III λλ1183–85 and N III λλ1748–52. The N IV λ1718 line was excluded because it is affected by the wind and N V λ1240 is X-ray sensitive, and hence not suitable as an abundance diagnostic.

Oxygen. ϵ Ori shows a variety of O II and O III lines – our abundance analysis was based on: O III λλ4368, 5594 and O II λλ4077, 4134, 4663. Other lines that show abundance dependence are those in the blend O II-III λ4415–18. The UV lines commonly used for abundance diagnostics are O IV λλ1338–43 and O III λλ1150–54 but they show only a weak abundance dependence in the models. O V λ1371 was not detected in the UV spectra of ϵ Ori.

Silicon. The silicon abundance was estimated using only Si III and Si IV lines since Si II lines were not detected. The triplet Si III λλ4552-67-74 and Si III λ5738 were useful as well as Si IV λλ4089, 4116. No UV lines were used for the analysis due to their strong dependence on the wind parameters.

Iron. We only used UV Fe lines for estimating its abundance. The iron features Fe V λλ1360 - 1385, Fe IV λλ1550 - 1700, and Fe III λ1800–1950 were used. Again, it is important to have a reliable value for temperature to get an accurate abundance estimation.

4.2.5 Rotation and macroturbulence

We account for the influence of rotation on the stellar spectrum in two ways. First, we convolve a rotational broadening profile with the synthetic spectrum. This method assumes solid rotation of both the star and wind, and that the line profile does not vary from the centre to the limb (Gray 2008). Wind-free line profiles were used to estimate the projected rotation velocity ($v_{\rm rot}\sin i$).

In the second technique we calculate the synthetic spectrum using the 2D code developed by Busche & Hillier (2005). This code computes the radiative transfer through the photosphere and wind using an axisymmetric geometry and allows for rotation of the star. Recently, Hillier et al. (2012) studied the application of the code to optical line profiles of O stars. They showed that while the convolution method that is commonly used to allow for rotation is adequate for photospheric absorption lines, it fails for lines influenced by photospheric emission, or for lines with wind emission contribution. For the diagnostic lines Hα and He II λ4686, it is important that the influence of rotation be correctly modelled.

Because the rotation rate of ϵ Ori is low we can use the same simplifications as Hillier et al. (2012) – we assume the rotation does not affect the density structure, temperature and surface gravity. We also assume that the star rotates as a solid body below $v(r)=20$ km s^{-1} and the angular momentum about the centre is conserved above that value.

Finally, in order to compare the synthetic spectra with the optical observational data, it is necessary to take into account instrumental broadening and macroturbulence. Instrumental broadening was taken into account by convolving a Gaussian profile of 4.0 km s^{-1} from NARVAL spectral resolution. Macroturbulence broadening

was included through a convolution assuming an isotropic Gaussian distributed velocity field. The value of the full width at half maximum of such a distribution in km s^{-1} was estimated using the wings of isolated wind-free metallic lines.

4.3 Wind parameters

The parameters that describe the stellar wind are those that have to do with the wind velocity law (β and v_∞), the mass-loss rate ($\dot{M}$), the filling factor (f_∞, $v_{\rm cl}$) and the wind turbulent velocity ($\xi_{\rm max}$). All of these influence spectral features in the UV, optical, and X-ray bands. Some line profiles are strongly influenced by two or more of the parameters. For example, the strength of Hα is highly sensitive to both the mass-loss rate and filling factor, and its profile shape is sensitive to β. Thus, these wind parameters need to be determined simultaneously using several spectral features from different ions and species.

The value of $\dot{M}$ is first constrained using the Hα strength for $f_\infty = 1.0$, 0.1, 0.05 and 0.01 ($f_\infty = 1.0$ means smooth wind). A consistency check was then done using the UV line profiles of C IV $\lambda\lambda$1548,1551, N V λ1240, Si IV $\lambda\lambda$1394,1403 and C III λ1776, which showed only a weak dependence on mass-loss rate (in our models) when compared with Hα.

The clumping factor (f_∞) is determined using S IV $\lambda\lambda$1062,1073, P V $\lambda\lambda$1118–28 and N IV λ1718. The parameter $v_{\rm cl}$ has a slight influence on the Hα shape, so its value is adjusted only to improve the line profile once the $\dot{M}$ is estimated from line strength. Hillier (2003) suggested that its value should be less than 100 km s^{-1}. Likewise, Bouret et al. (2003) (see also Bouret et al. 2005) suggested that clumping should start close to the photosphere ($v_{\rm cl} \sim$ 30 km s^{-1}). For the models in this work, we used $v_{\rm cl}$ values from 20 to 100 km s^{-1}.

The velocity profile parameters (v_∞, β) were constrained using UV P Cygni line profiles and the Hα line profile. The Hα profile shape is strongly sensitive to β – we used values from 1.0 to 2.4 to find the best profile. Once we alter β it is necessary to re-tune the mass-loss rate to match the Hα intensity.

In the same sense, v_∞ was estimated using the blue wing of the P Cyg profile of C IV $\lambda\lambda$1548,1551 and the Si IV $\lambda\lambda$1394,1403 profile. As the shape of that wing is also affected by the wind turbulence $\xi_{\rm max}$ we tune v_∞ and $\xi_{\rm max}$ simultaneously.

4.4 X-ray wind parameters

As X-rays propagate through the wind they can be absorbed and photoionize the gas. The effect on an X-ray line is an attenuation of the profile on the red side, because the red-shifted photons from the rear hemisphere encounter a longer path length through the wind than the blue-shifted photons from the front hemisphere (Macfarlane et al. 1991; Owocki & Cohen 2001). Since the X-ray opacity varies with wavelength the influence on line profiles varies with wavelength. Furthermore, the strength of the effect depends primarily on the wind column density and hence the mass-loss rate. Thus, with a known opacity distribution, it is possible to estimate the mass-loss rate from the observed X-ray lines (Cohen et al. 2014a).

In this work we utilize X-ray cross-sections from Verner & Yakovlev (1995). The spatial variation in opacity is determined by the velocity law and mass-loss rate. We use the same values estimated from the optical and UV data. Once the best fit is attained, the line profiles are checked for consistency. Previous $\dot{M}$ estimations from X-ray lines used individual line profiles (Oskinova, Feldmeier & Hamann 2006; Cohen et al. 2014a); in this work we use models for the whole X-ray spectrum. A similar approximation was developed by Hervé et al. (2013), but they used a fiducial radial dependence for opacity.

The effects of v_∞ and β on X-ray profiles have been studied by Cohen et al. (2010). Here, we use the same values obtained from the optical and UV analysis. We show below that β can influence R_0, and this gives us the opportunity to check our results against the instability wind models (Feldmeier et al. 1997; Runacres & Owocki 2002; Dessart & Owocki 2003, 2005) relating the wind acceleration with the shock formation region.

4.5 X-ray abundances

Once global best fit to the X-ray spectra is obtained, the abundances are adjusted so as to improve the fit of line ratios.

To compute the observed line strength ratios, the line fluxes were measured using Gaussian profiles and the statistical tools from XSPEC. The free parameters for each fit were the normalization factor and the line width (σ of each Gaussian). The line centre is generally fixed at its laboratory value, but when necessary it was shifted to match the peak of the observed line – it was not included as a free parameter in the fit. We will specifically focus on the CNO line ratios. Recently, Zsargó et al. (in preparation) showed that good choices are:

$$R({\rm N/O}) = \frac{{\rm Flux(N\ VII\ Ly}\alpha)}{[{\rm Flux(O\ VIII\ Ly}\alpha) + {\rm Flux(O\ VII\ He\text{-}Like)}]}, \quad (4)$$

and

$$R({\rm C/N}) = \frac{{\rm Flux(C\ VI\ Ly}\alpha)}{[{\rm Flux(N\ VII\ Ly}\alpha) + {\rm Flux(N\ VI\ He\text{-}Like)}]}, \quad (5)$$

which have a weak dependence on temperature and are good choices to test the consistency of our abundance values from the optical and UV analysis. New abundances can be estimated when the observed ratios are compared with the ones from our models.

5 RESULTS

5.1 Stellar parameters

The main stellar parameters that we estimated for ϵ Ori are shown in Table 4. Each row in the table corresponds to the parameters from the two different distances from the *Hipparcos* catalogues. The luminosity from the lower distance lies between those calculated by Crowther et al. (2006) [$\log(L_*/{\rm L}_\odot) = 5.44$] and Searle et al. (2008) [$\log(L_*/{\rm L}_\odot) = 5.73$] and is close to other estimates reported in the literature (e.g. Lamers 1974; Kudritzki et al. 1999; McErlean et al. 1999). The luminosity computed with the larger distance is the highest value reported and makes ϵ Ori one of the most luminous B-supergiants in the Galaxy. This value is almost twice the calibrated value found by Searle et al. (2008) for galactic B0 Ia stars (They used jointly their sample and that of Crowther et al. (2006).). A similar statement applies to the mass-loss rate and stellar radius (mass). Thus the distance of van Leeuwen (2007) makes ϵ Ori an unusual B0 Ia supergiant. For the analysis, we prefer to use the lower value in order to compare with the previous work on ϵ Ori that were undertaken assuming a distance closer to that of Perryman et al.

Fig. 1 shows the analysis of Balmer line wings and He I-II lines. We concluded that $\log g = 3.0$. We also found that for values greater than 3.05 and lower than 2.95 it is not possible to fit the Balmer

Table 4. Stellar parameters of ϵ Ori from optical and UV data.

Log ($L_*/L_\odot$)[a]	$T_{\rm eff}$ 10^3 (K)	log g	R_* $R_\odot$	M_* $M_\odot$	$\xi_{\rm min}$ km s^{-1}	$v \sin i$ km s^{-1}	$v_{\rm macro}$ km s^{-1}	$E(B-V)$ mag	d pc
$5.59^{+0.51}_{-0.20}$	27.0 ± 0.5	3.0 ± 0.05	28.6	30.0	15–20	40–70[b]	70–100	0.091 ± 0.01	412[c]
$5.92^{+0.32}_{-0.18}$	27.0 ± 0.5	3.0 ± 0.05	42.0	64.5	15–20	40–70[b]	70–100	0.091 ± 0.01	606[d]

[a]Error from distance uncertainties.
[b]Value computed using the convolution method.
[c]*Hipparcos* catalogue (Perryman et al. 1997).
[d]*Hipparcos* catalogue (van Leeuwen 2007).

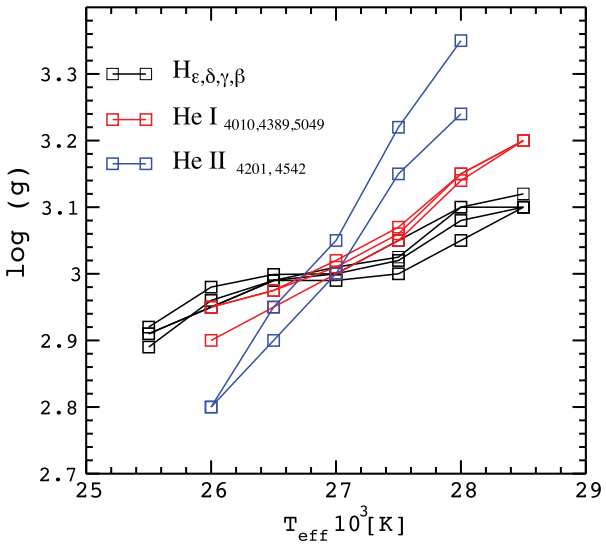

Figure 1. Constraints on $T_{\rm eff}$ and log g. Shown are fits to the Balmer line wings (black), the equivalent width of He I (red) and He II (blue) lines.

and He I-II lines consistently. Thus, we estimate an error of 0.05 for log g.

Fig. 2 shows the analysis for the ionization balance of He I-II and Si III-IV. The ionization balance of He I-II yields an effective temperature of approximately 2.65×10^4 to 2.68×10^4 K while the Si III-IV ionization balance yields a value $\sim 2.68 \times 10^4$ to 2.75×10^4 K. From these results we concluded that the effective temperature of ϵ Ori is $T_{\rm eff} = 27\,000 \pm 500$ K. In the UV, Si III λ1312 shows a strong dependence on temperature. This line yields a slightly lower temperature of $T_{\rm eff} = 26\,200$ K. Nevertheless, Fe IV-V lines and the O IV λλ1342,1343 lines support a value of 27 000 K. The Si III-IV λλ1417,1416 lines provide a temperature estimate of 27 500 K.

Photospheric microturbulence velocity ($\xi_{\rm min}$) was estimated to be between 15 and 20 km s^{-1} using He I lines. The silicon triplet (4554–4576 Å) suggests a $\xi_{\rm min}$ close to the lower limit, 15 km s^{-1}, while the UV Si III multiplet indicates a microturbulence closer to 10 km s^{-1}(Fig. 3). The variations do not change the reported limits for temperature and gravity.

Fig. 3 shows the line profiles for optical and UV Si III lines. The models correspond to three values of the microturbulent velocity: 20 km s^{-1} (red), 10 km s^{-1} (blue) and 5 km s^{-1} (green). We found divergence between the UV and optical silicon lines – the UV (Si III λλ1290–1310) complex suggests $\xi_{\rm min} \sim 10$ km s^{-1} while the optical triplet Si III λλ4550–4580 requires a value of $\xi_{\rm min} \sim 20$ km s^{-1}. Furthermore, the Fe IV λλ1450–1500 and Fe IV λλ1600–1700 lines rule out $\xi_{\rm min}$ lower than ~ 10 km s^{-1}.

The discrepancy between UV and optical Si III lines can be overcome by increasing the silicon abundance by a factor of ∼1.2 with $\xi_{\rm min} = 15$ km s^{-1}. However, such a value is incompatible with other optical lines (e.g. N III λ4098 and C III λλ4648–4654).

The rotation and macroturbulence velocities were estimated simultaneously from fitting the line shapes. We estimated values of 40–70 km s^{-1} for rotation and 70–100 km s^{-1} for $v_{\rm macro}$. That rotation value is lower than previously reported [$v \sin i = 91$ km s^{-1} by Howarth et al. (1997)]. However, upon close examination we found this rotation rate accurately fits some optical line profiles, such as those belonging to Si III λ4554–4576. Rotation is analysed in Section 5.7.

5.2 Wind parameters

We calculated models for four different values of filling factor (f_∞). The best-fitting parameters for each of these models are shown in Table 5. We use capital letters as reference for the subsequent analysis. The best synthetic spectra for each filling factor from UV to optical together with data are shown in Appendix A.

5.2.1 *Mass-loss rate*

Because of the strong sensitivity of the Hα line profile to the mass-loss rate, it is possible to attain high precision for this parameter through fitting its line strength. We found $\dot{M}/\sqrt{f_\infty} \approx 1.6 \times 10^{-6}$ M$_\odot$ yr^{-1} for ϵ Ori ($d = 412$ pc). The mass-loss rate for each filling factor is shown in Table 5. As expected, $\dot{M}/\sqrt{f_\infty}$ is almost independent of f_∞, and is lower than the value $\dot{M} \sim 2 \times 10^{-6}$ M$_\odot$ yr^{-1} estimated by Searle et al. (2008) and Crowther et al. (2006). The main reason for the discrepancy is their adopted lower values for β (1.1 and 1.5, respectively). A lower β value yields lower densities in the Hα formation region, and hence a higher mass-loss rate is required to fit the line emission. As these values were computed using mainly Hα, its variability will increase the uncertainty of the mass-loss rate. Morel et al. (2004) and Thompson & Morrison (2013) reported Hα variability in its shape profile and strength. The results shown here are based on data collected on a specific date, and do not show Hα variability during observations. We changed the mass-loss rate in order to obtain the strongest and the weakest line from Thompson & Morrison's profile. The corresponding values are 4.8×10^{-7} and 2.8×10^{-7} M$_\odot$yr^{-1}, respectively (assuming $\beta = 2$, $f_\infty = 0.05$ and $d = 412$ pc). The variation is approximately 30 per cent about our derived mass-loss rate of 3.6×10^{-7} M$_\odot$yr^{-1}. This shows that small changes in $\dot{M}$ yield large changes in the Hα profile. A full variability analysis is necessary to improve our conclusions about $\dot{M}$ for ϵ Ori, but this kind of analysis is beyond the scope of this paper.

In our analysis we did not include the infrared (IR) and radio spectral regions, but we can compare our results with those from previous studies. Blomme et al. (2002) used radio fluxes from 3.6

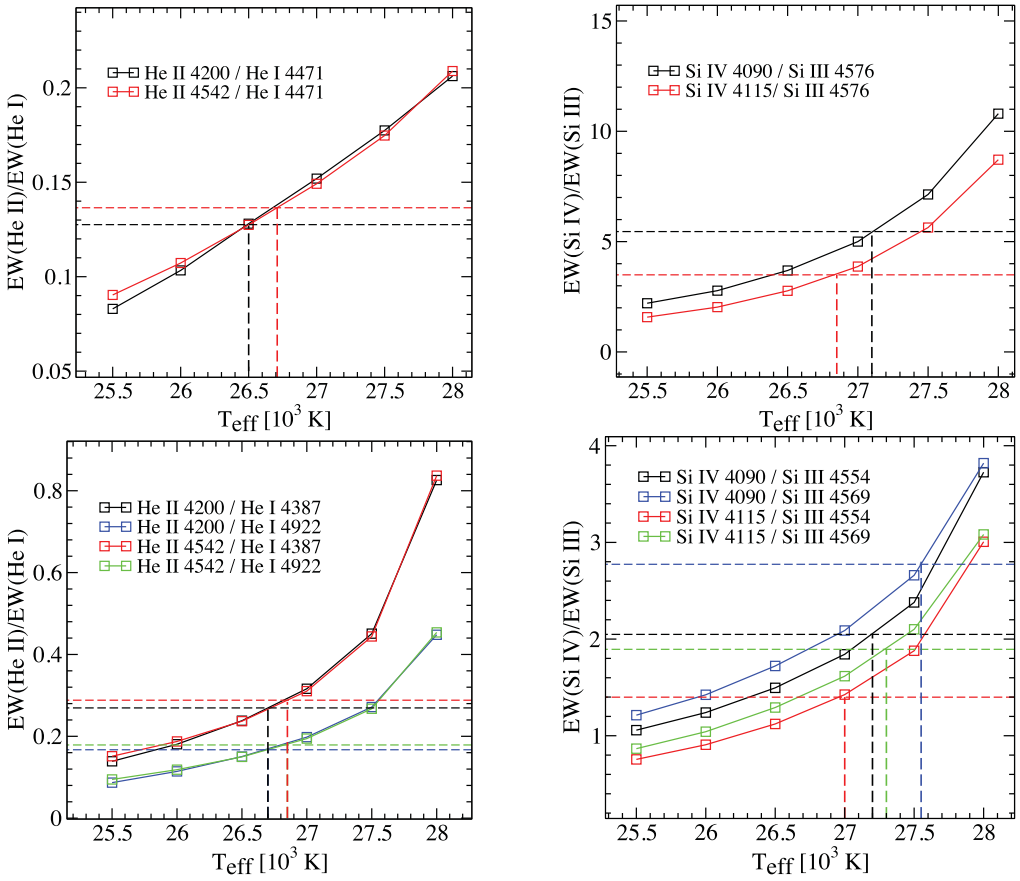

Figure 2. Ionization balance for He I–II and Si III–IV. The ratio of EWs for selected pairs of He and Si lines are shown for models with $\log g = 3.0$ and $T_{\rm eff} = 2.55$–2.8×10^4 K. Each square represents the model that matches the observed ratio of the EWs of the lines. The horizontal dashed lines show the EW ratios measured from optical data, while the vertical dashed lines show the projection of the matching model EW to the temperature axis. We estimated the measured EW ratio errors. The maximum is around 1 per cent, which would influence our lower temperature limit by $\lesssim$100 K.

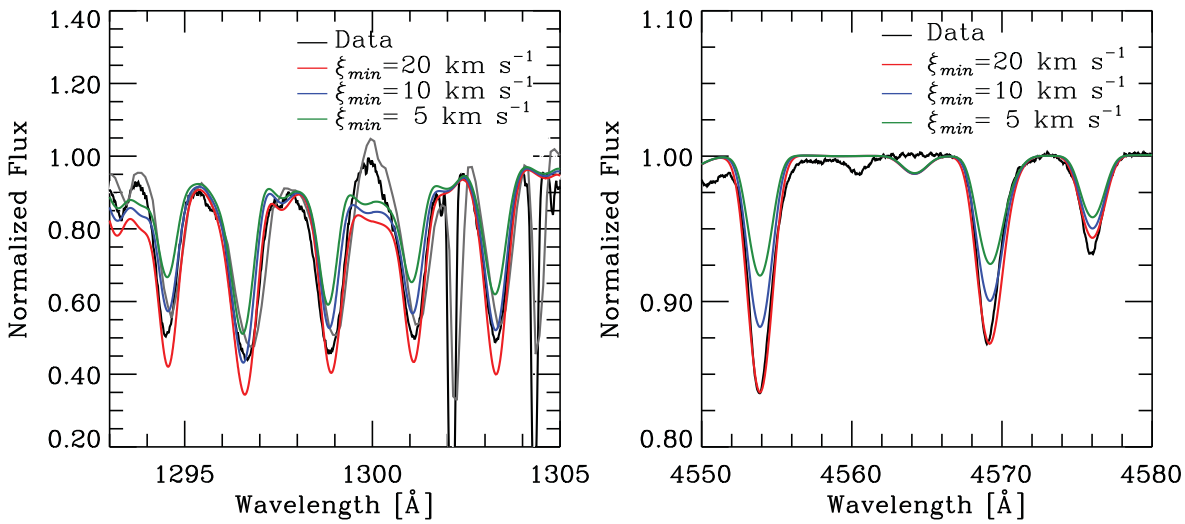

Figure 3. Dependence of UV and optical Si III lines on photospheric microturbulence ($\xi_{\rm min}$). In the left panel, the black line represents the GHRS data and the grey line *Copernicus* data. Profiles for three photospheric microturbulent velocities are shown: 20 km s^{-1} (red), 10 km s^{-1} (blue) and 5 km s^{-1} (green).

and 6.0 cm and computed $\dot{M} \sim 1.66 \times 10^{-6}$ M$_\odot$ yr^{-1} assuming a smooth wind. This is consistent with our estimate, but only if clumping persists into the radio region (our model fluxes at 6.0 cm is ∼0.7 mJy, while the mean of those reported by Blomme et al.'s is ∼0.74 ± 0.13. mJy.). Models by Runacres & Owocki (2002) indicate that structure can persist into the radio region and may influence radio diagnostics. On the other hand, Puls et al. (2006) found a difference between stars with strong and weak winds. For strong winds their analysis suggested that wind clumping declined into the radio region while for weak winds they found similar clumping in

Table 5. Wind parameters of ϵ Ori from optical and UV data. The mass-loss rate for both *Hipparcos* distances is given.

Model	f_∞	$\dot{M}/\sqrt{f_\infty}$[a] $M_\odot yr^{-1}$	$\dot{M}/\sqrt{f_\infty}$[b] $M_\odot yr^{-1}$	v_∞ km s^{-1}	β	ξ_{max} km s^{-1}	v_{cl} km s^{-1}
A	0.1	1.55×10^{-6}	2.70×10^{-6}	1800	2.0	200	40
B	0.05	1.66×10^{-6}	2.80×10^{-6}	1800	2.0	200	30
C	0.01	1.75×10^{-6}	2.90×10^{-6}	1800	2.0	200	20
D	1.0	1.40×10^{-6}	2.55×10^{-6}	1800	2.0	200	–

[a] *Hipparcos* catalogue (Perryman et al. 1997) ($d = 412$ pc).
[b] *Hipparcos* catalogue (van Leeuwen 2007) ($d = 606$ pc).

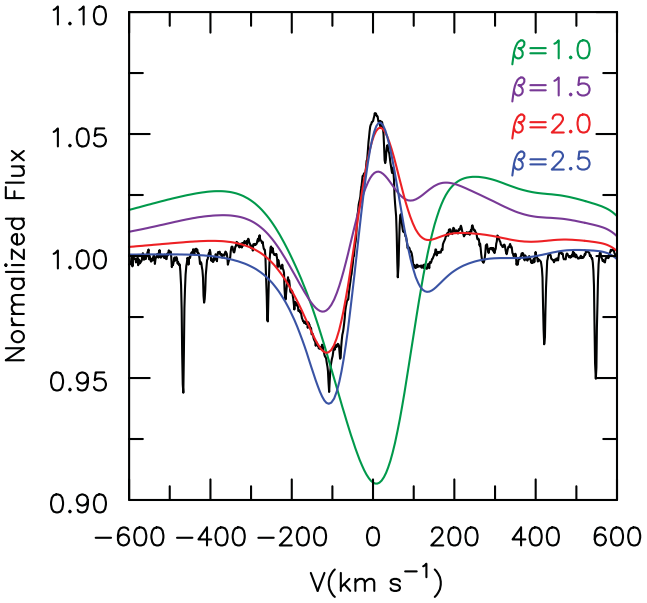

Figure 4. Hα profiles for different β values: 1.0 (green), 1.5 (purple), 2.0 (red) and 2.5 (blue). Black line represents the optical data. Each line profile was computed with the $\dot{M}$ that matches the observed line strength.

the inner and outer wind. In future work radio and millimetre fluxes should be incorporated into the analysis.

Using IR observations Repolust et al. (2005) obtained $\dot{M}/\sqrt{f_\infty} = 3.7 \times 10^{-6}$ $M_\odot$ yr^{-1} while Najarro et al. (2011) derived $\dot{M}/\sqrt{f_\infty} = 2.0 \times 10^{-6}$ $M_\odot$ yr^{-1} (for the comparisons we scaled the reported values to our distance and v_∞). The $\dot{M}$ derived by Najarro et al. is consistent with our estimate while that of Repolust et al. is a factor of ~ 2 higher.

UV lines are less sensitive than Hα to changes in $\dot{M}/\sqrt{f_\infty}$. Therefore, we use UV lines only to confirm our Hα values. Moreover, UV line strengths also depend on ionization structure and some of them also on the X-ray emission (e.g. N V and C IV). The X-ray independent and non-saturated UV line C III λ1176 confirmed the $\dot{M}$(Hα) values. Si IV λλ1394–1402 was not well reproduced, likely because of vorosity–porosity effects, so it was disregarded in the analysis (Section 6).

5.2.2 *Velocity profile*

The wind acceleration parameter (β) strongly affects the Hα profile (Hillier 2003). The Hα profiles calculated for $\beta = 1.0$, 1.5, 2.0 and 2.2 are shown in Fig. 4. From this figure, we concluded that the better β value is around 2.0 (values lower than 1.8 or higher than 2.2 were unable to reproduce the profile). This value is higher than others previously calculated for early B-supergiants (e.g. Kudritzki et al. 1999; Crowther et al. 2006; Searle et al. 2008). For each β we explored a wide range for $\dot{M}/\sqrt{f_\infty}$; however we were unable to match the observed line profile for low β values.

Crowther et al. ($\beta = 1.5$) used two sets of optical data for ϵ Ori, but the line shape was not reproduced in either case. They obtained high-velocity wing emission that is not detected, and they were unable to reproduce the blue absorption observed in the Hα profile.

Searle et al. ($\beta = 1.1$) do not show their Hα profile; we tried to fit this line with their β value by tuning other wind parameters but we were unable to reproduce the line shape with such a low β value.

In the above works other Galactic early-type B-supergiant stars were also analysed. The derived β values are between 1.0 and 1.5. For Small Magellanic Cloud (SMC) B0-B1 supergiants, Trundle et al. (2004) also found β values lower than ours. Evans et al. (2004) analysed two B0 Ia stars within a sample of supergiants from the Magellanic Clouds: AV235 and HDE 269050. They found β parameters of 2.50 and 2.75, respectively.

Spectral variability of Hα could be one reason for the discrepancy between our values and those derived from previous works. Thompson & Morrison (2013) reported profile variability on a time-scale of weeks. This variability is still not understood (see also Martins et al. 2015). An alternative to be investigated in the future is a different radial dependence for the filling factor. Runacres & Owocki (2002) predicted that the clumping factor ($f_{cl} = 1/f$) grows until 10–50 R_* and then falls in the outer wind regions. However, Puls et al. (2006) show that for denser winds high clumping factors are present close to the stellar surface. ϵ Ori does not show a high mass-loss rate, but a different clumping distribution should be investigated in combination with other β values.

The v_∞ and ξ_{max} parameters were estimated together using the blue absorption wing of UV lines, especially C IV λ1550 and C III λ1175. We found that the value of v_∞ lies between 1700 and 1800 km s^{-1}, while the wind turbulent velocity is $\xi_{max} \sim$200 km s^{-1}.

The values calculated here are between the previous ones calculated by Crowther et al. (2006) and Searle et al. (2008) (1600 and 1910 km s^{-1}, respectively). The C III λ1175 profile rules out a value of 1600 km s^{-1} for v_∞, since a value of $\xi_{max} \gtrsim 300$ km s^{-1} is necessary in order to fit the blue absorption wing. Such a high value for ξ_{max} distorts the Si IV λ1400 profile and the C IV λ1550 blue absorption wing.

5.2.3 *Clumping*

Besides the mass-loss rate, we also changed v_{cl} (the point where the clumping starts) aiming to optimize the Hα profile. The best values for v_{cl} for each f_∞ are shown in Table 5 and are between

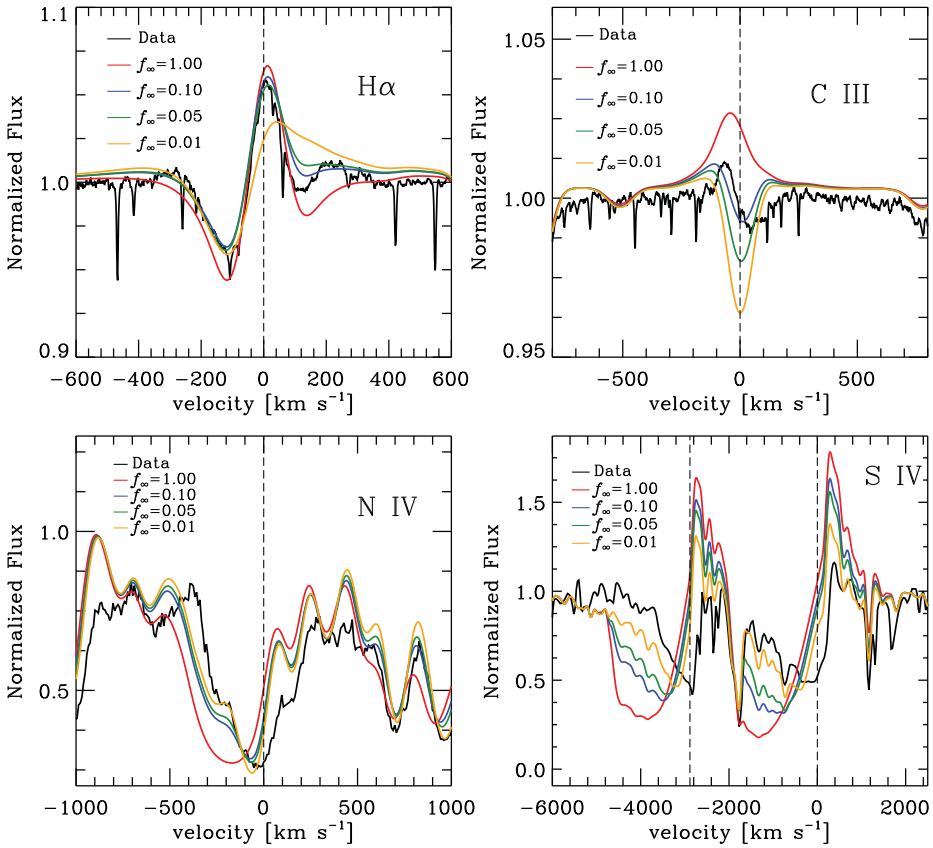

Figure 5. Shown is the effect of clumping on selected optical and UV lines. Upper panels correspond to the optical lines Hα and C III λ5697, while the lower ones correspond to UV lines S IV $\lambda\lambda$1062,1073 and N IV λ1718.

20 and 40 km s^{-1}. Fig. 5 shows the effect of f_∞ on different lines in the optical and UV. We found that S IV $\lambda\lambda$1062,1073 and N IV λ1718 yield a low value for f_∞ ($\leq$0.01). The same was found for P V $\lambda\lambda$1118–28 (not shown in the figure). On the other hand, the optical lines yield a moderate value between 0.05 and 0.1. These discrepancies cannot be corrected by altering the mass-loss rates without spoiling the Hα profile. It is possible to alter the abundances until the model fits the lines, but the derived values for a reasonable value for f_∞ are too low to be plausible, especially for sulphur.

5.3 Abundances from UV and optical

We chose model 'A' to estimate the abundances of CNO, Si and Fe. The lines selected for estimating the abundances are not affected by wind emission, hence it is irrelevant which model, from Table 5, we choose. Solar abundances for Si and Fe fit the optical and UV spectra to within 10 per cent. Because of this, we fixed their abundances to solar values and concentrated our analysis on CNO abundances. Nevertheless, as it was noted above, a silicon abundance of 1.2 Si$_\odot$ helps to reconcile the fit to the UV and optical Si III multiplets.

Fig. 6 shows three panels. In each of these panels the *y*-axis shows the abundance estimate obtained from each transition and the *x*-axis shows the line wavelength. The numerical abundances are relative to hydrogen, expressed as: $\log(N_X/N_H) + 12$. The filled black line represents the mean value (simple average) while the dashed lines represent the standard deviation of those measurements.

Table 6 shows the mean CNO abundances and their standard deviations, the N/C and N/O abundance ratios, and the corresponding solar values. These ratios are calculated as: [N/(C,O)] $= \log(N_N/N_{(C,O)})_* - \log(N_N/N_{(C,O)})_\odot$. The other three columns show previous abundance estimates from Crowther et al. (C06) and Searle et al. (S08).

Our values for [N/(C,O)] show a small nitrogen enhancement and carbon and oxygen depletion. This provides evidence for CNO processed material at the star surface. Nevertheless, when compared with C06 and S08, our values are closer to the solar ones.

The abundance determinations typically scatter within a factor of 2 either side of the mean, as shown in Fig. 6. Fig. 7 shows the sensitivity of several lines to the abundance. For instance, C III λ4070 requires half of the abundance predicted by C III λ4650. Similarly the O II $\lambda\lambda$4663 abundance is 2.5 times larger than that obtained with O II $\lambda\lambda$4700,4707.

The possible causes of the abundance discrepancies are many – complex NLTE effects, deficiencies in the atomic models, blending, issues related to microturbulence and macroturbulence. For example, it was pointed out by Nieva & Przybilla (2006) that NLTE effects can cause discrepancy between the abundances estimated using C II lines 4267 Å and 6587–82 Å. We did not find strong discrepancies among these lines – the difference is not larger than 0.2 dex. Likewise, complex NLTE effects could affect the abundance estimates of other lines such as C III (Martins & Hillier 2012) and N II–IV (Rivero González, Puls & Najarro 2011; Rivero González et al. 2012a,b).

5.4 Wind parameters from X-rays

We performed the fit procedure as described in Section 4.1.2, using the *Chandra* and *XMM–Newton* data simultaneously. The

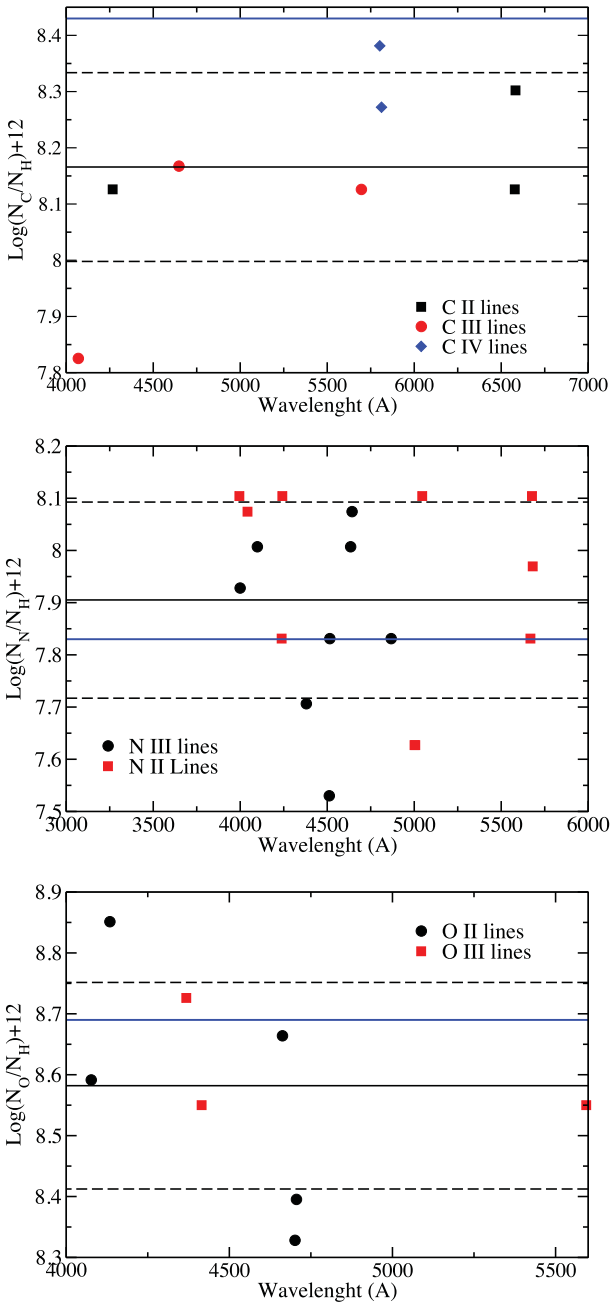

Figure 6. Abundances for CNO. The dots show the abundance that fits each line for each ion and species. The black line is the mean of those abundances, the dashed lines are the mean ± the standard deviation and the filled blue line represents the solar value.

Table 6. CNO abundances from optical and UV data. [N/C,O] = $\log(N_N/N_{C,O})_* - \log(N_N/N_{C,O})_\odot$.

Species	This work	σ(dex)	S08	C06	Solar
C	8.16	0.16	7.66	7.95	8.43
N	7.90	0.18	7.31	8.15	7.83
O	8.58	0.17	8.68	8.55	8.69
Si	7.51	0.04	7.51	7.51	7.51
Fe	7.50	0.04	7.50	7.50	7.50
[N/C]	+0.33	–	+0.26	+0.8	0.00
[N/O]	+0.15	–	-0.49	+0.5	0.00

results for each of the models described above (A, B, C and D) are shown in Table 7. For each model we found that low temperature (∼1–3 × 10^6 K) plasmas are necessary to account for the N VII Lyα, N VI Heα and C VI Lyα lines, as well as the He-like line of Ne IX Heα. Similarly, a hot component is needed to account for Si XIII, Mg XII and Mg XI lines. The Si XIV Lyα at 6.18 Å is not detected by *Chandra*, and hence the hottest plasma temperature is less than 1 × 10^7 K. These temperatures are consistent with the distribution of heating rates computed by Cohen et al. (2014b) for ϵ Ori. They show that ϵ Ori has low heating rates for $T \gtrsim 10^7$ K.

Figs 8 and 9 show the *Chandra* and *XMM–Newton* data with the models A (green), B (blue), C (orange) and D (red), respectively. The fits are reasonable for most lines, except for Ne X λ12.13 which is too weak in all our models. The fit of this line is strongly coupled to the fitting of the Mg XI–XII lines – better Ne X line profiles were obtained when those lines were excluded from the fits but the model Mg lines are too strong. The whole fit improves if we lower the Mg abundance by approximately 10 per cent. On the other hand, Drake & Testa (2005) and Cunha, Hubeny & Lanz (2006) have suggested that the currently accepted solar abundance of neon might be underestimated. We computed models increasing the Ne abundance by 40 per cent, and although the Ne X λ12.13 profiles improve, the emission in the Ne He-like triplet is overestimated.

Table 7 shows the spatial distribution of the emitting plasmas. Typically the coolest plasma is found to exist at larger radii than the hottest plasma. Specifically, for 10^6 K plasma R_0 is around 4–4.9 R_*, for the 2–3 × 10^6 K plasma R_0 is between ∼3 and 4.7 R_*, and for the 7 × 10^6 K plasma $R_0 \sim 2.1$–2.9 R_*. We note that the onset radii are above the height where clumping starts [v_{cl} = 20–40 km s^{-1} = $v(r \sim 1.12$–$1.23\ R_*)$]. The same result was found by Cohen et al. (2011) in their analysis of HD 93129A – the estimated onset radii were larger than R_{cl}.

The present analysis allows for contributions from different plasmas (T_X and R_0) to each X-ray line. Here, the principal lines in the *Chandra* and *XMM* wavelength range are fitted consistently with the same model. Thus, we found that short-wavelength lines have flux contributions from hot plasmas, unlike long-wavelength lines that mainly have contributions from colder plasmas. The same trend was found by Hervé et al. (2013) (their fig. 4) in their analysis of the RGS spectrum of ζ Pup.

The findings indicate that the shortest wavelength lines start to be emitted from regions close to the stellar surface in the wind, while the longer wavelength lines originate from the outer regions. This result is confirmed by line width measurements – lines with a higher wavelength have larger line widths (Tables 8 and 9).

Waldron & Cassinelli (2007) argued that this trend, found in some supergiants, does not indicate that the cooler shocked plasma is formed only in the outer wind regions. Rather, the inner cool gas is not seen due to optical depth effects. In other words, the wavelength dependence of continuum X-ray optical depth means that long-wavelength photons produced close to the surface are absorbed by the optically thick wind. Cohen et al. (2014a) emphasized optical depth effects as an explanation. They did not find a significant trend in their sample of O stars (ϵ Ori included). However data for some stars are suggestive of longer wavelength lines from lower-temperature plasma being formed farther out in the wind. Fig. 10 illustrates this point. It shows curves of the radius where the continuum X-ray optical depth equals unity, $r(\tau_x = 1)$, and

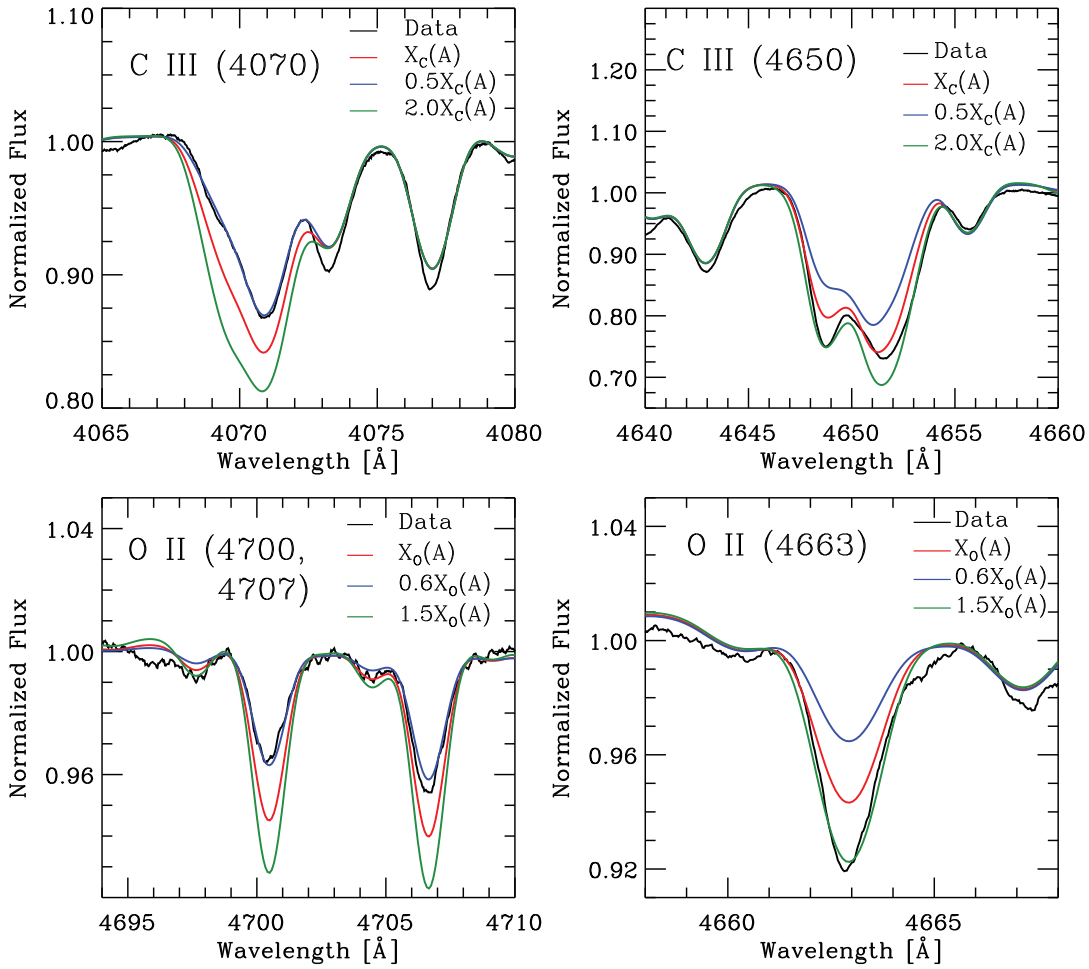

Figure 7. Abundance discrepancy from lines of the same ion: C III (upper panels) and O II (lower panels). C III λ4070 requires half the abundance needed by C III λ4650 while the O II λ4663 abundance is 2.5 times larger than that found from O II λλ4700,4707.

the wavelengths of the main H-like and He-like lines. Utilizing Fig. 10 in conjunction with Table 7 it is apparent that every 'observed' plasma exists above the $r(\tau_x = 1)$ where the transmission factor is high for each wavelength, as was pointed out by Leutenegger et al. (2010). Despite the high R_0, we estimate that ∼70 per cent of the emitted X-rays are absorbed by the wind – the X-ray absorption is very significant for $\lambda \gtrsim 12$ Å.

Figs 11 and 12 show the calculated line profiles for some H-like and He-like X-ray lines together with data from *Chandra* and *XMM*. H-like profiles are centred at the red component of the doublet, whilst He-like profiles are centred at the red component of the intercombination doublet. A visual inspection shows that the observed lines are slightly blue-shifted, and that every model reasonably reproduces the profiles, with the exception of model 'D' (red line). This is especially clear when we look at the O VIII profile.

In order to clarify which models match the observations we calculated the '*C*' statistics for each H-line and He-like line model profile. To do this we allow the flux for each model profile to be a free-parameter, and choose the scaling that minimizes the *C* statistic. The results are shown in Tables 8 and 9 for *Chandra* and *XMM* data, respectively. From the values, we confirm that the smooth wind model (model 'D') can be ruled out based on the fit to O VIII and O VII ($\Delta C \gg 6.63$ when compared to the minimum among the other values of the same line), although the Ne IX, N VII and C VI lines also have inferior-*C* statistics for model D. The other models, and other lines, have similar values for the *C* statistics, and can be considered statistically indistinguishable.[9]

From the results described above, we conclude that the mass-loss rate required to fit the X-ray spectrum of ϵ Ori is $\lesssim 4.5 \times 10^{-7}$ $M_\odot$ yr^{-1}, which confirms the UV and optical results that the ϵ Ori wind is clumped. Furthermore, these values of mass-loss rate agree with those reported by Cohen et al. (2014a) for the same star using exclusively *Chandra* data. Cohen et al. (2014a) computed two values for the mass-loss rate of ϵ Ori: 6.5×10^{-7} $M_\odot$ yr^{-1} and 2.1×10^{-7} $M_\odot$ yr^{-1}. The former comes from excluding from their analysis the lines (three lines from 10) which possibly are affected by resonance scattering (Leutenegger et al. 2007), while the lower value results from including all of the lines of their spectrum. As pointed out above R_0 values move the X-ray line formation region out of the absorbed part of the inner wind, making it unnecessary to include the resonance scattering to make more symmetric lines. Including resonance scattering effects in the analysis could have an influence on the computed β and R_0 values, but not in a strong way due to the low density of ϵ Ori's wind (which is less than that of ζ Pup).

[9] In our first approach we scaled each model profile to have the same peak value. While the *C* statistics were higher than those tabulated in Tables 8 and 9, the same trends are seen.

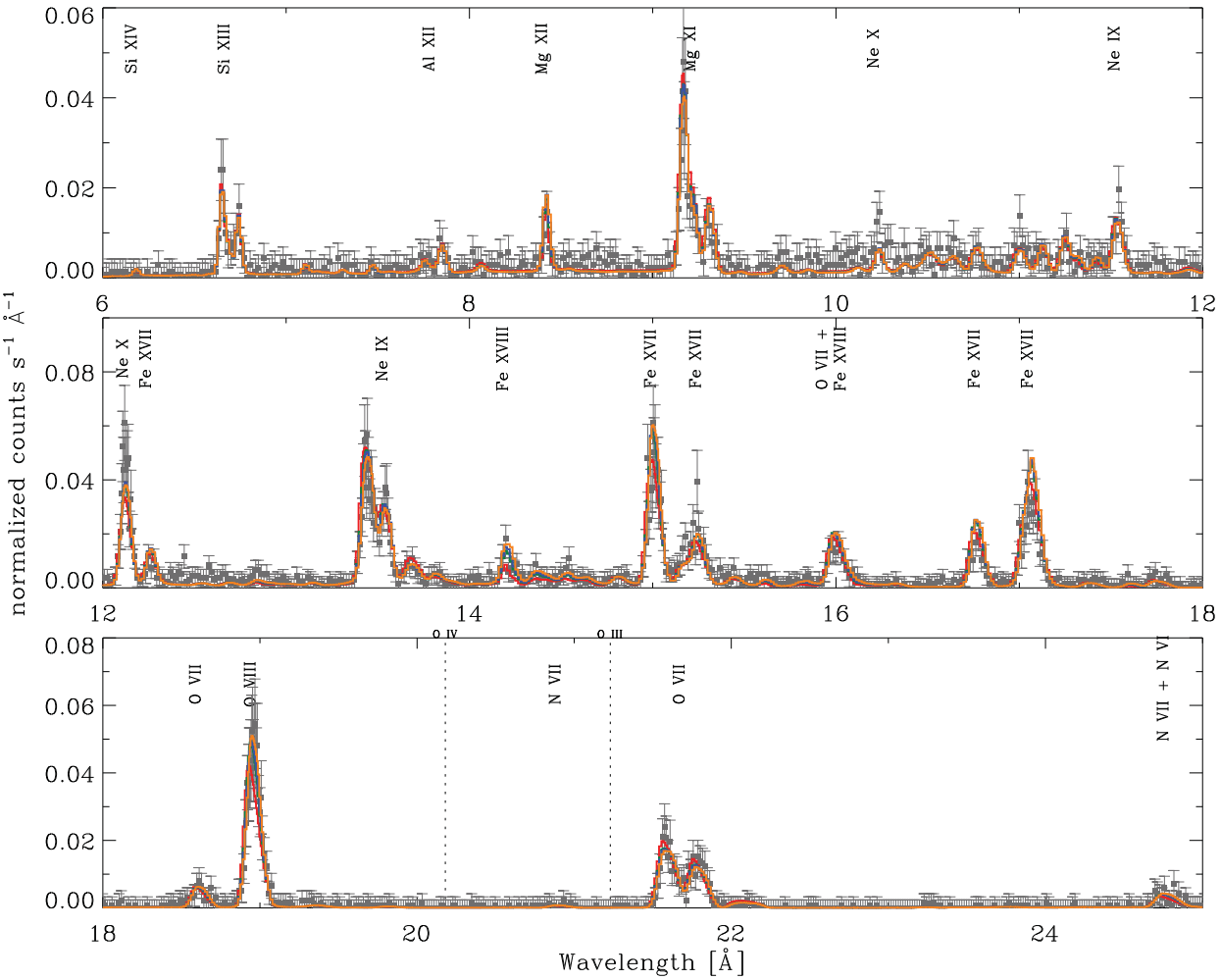

Figure 8. *Chandra* data (grey squares with error bars) and best X-ray models for A (green), B (blue), C (orange), and D (red). Dotted lines show the K-shell ionization threshold for O III and O IV. The models are indistinguishable except for a few lines.

Models using a different wind acceleration parameter ($\beta = 1.0$, 1.2) were also calculated. Wind and photospheric parameters from model 'A' were adopted. For short wavelengths ($\lambda \lesssim 14$ Å) the model yields profiles that cannot be distinguished from the $\beta = 2$ model. But for longward wavelengths a better fit is provided by the $\beta = 2$ model. Specifically, the models fail to reproduce the He-like O VII line, and the Lyα lines of N VII and O VIII. For this set of lines the model profiles are too asymmetric when compared with the data. Quantitatively, the 'C' values increase ∼20–100 per cent for models with $\beta = 1$–1.2 when compared with $\beta = 2$ profiles (e.g. $\Delta C \sim 45$ in the case of Lyα O VIII). In the case of He-like N VI and Lyα C VI lines the increase in 'C' is approximately 5–10 per cent ($\Delta C \sim 3.0 - 6.0$).

The plasma temperatures were fitted again as described in Section 4.1.2. The lower temperatures are the same as those calculated above, but a better fit was achieved by switching the hottest plasma to 8×10^6 K. The onset radii are closer than those from the model with $\beta = 2$ because models with lower β yield higher velocities in the region from $R = 1.1$ to 6.1 R_*. The coolest plasma (10^6 K) has $R_0 = 2.16$ R_*, the plasma of 2×10^6 K has $R_0 = 6.1$ R_*, while the plasmas of 3×10^6 K and 8×10^7 K have R_0 values of 1.9 R_* and 1.4 R_*, respectively.

5.5 Abundances from X-rays

The metal abundances, relative to hydrogen, could be estimated using the continuum emission relative to line emission. But in the case of *XMM* data, most of the spectral range is contaminated by line emission. However, a narrow region around the nitrogen lines shows weak or no lines. The modelled continuum in this region is almost 50 per cent below that observed. To fit the continuum it would be necessary to both scale the model emission measures and lower the metal abundances by approximately 50 per cent in order to preserve the fit to the lines. By limiting the fit to the nitrogen lines region, a good match for both the continuum and those lines can be found. However, most of continuum comes from the hottest plasma ($T_X = 7 \times 10^6$ K), which spoils the fit to the shortward wavelength spectrum. Furthermore, as it is shown in Figs 8 and 9 the shortward continuum is fitted well by our models. This discrepancy could be due to a lack of pseudo-continuum weak lines in APEC as suggested by Zsargó et al. (in preparation).

For the reasons exposed above, it was not possible to derive metal abundances relative to hydrogen – only the relative abundances among metals. We searched for some trends by measuring the fluxes for the main X-ray metal lines from the data, and compared them to the corresponding model fluxes.

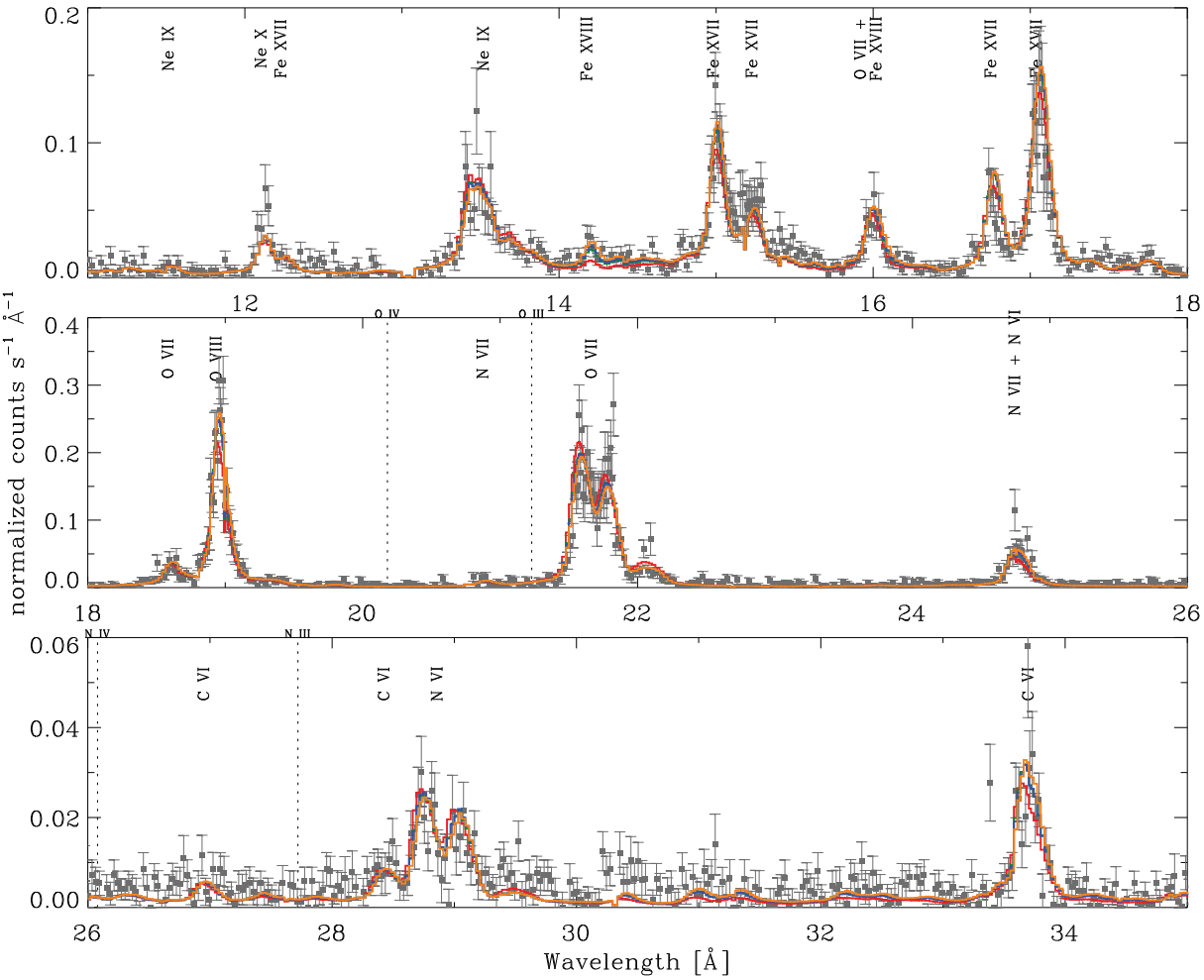

Figure 9. *XMM–Newton* data (grey squares with errors bars) and best X-ray models for A (green), B (blue), C (orange), and D(red). Dotted lines show the K-shell ionization threshold for O III, O IV, N III and N IV.

Table 7. Plasma parameters for the best models that fit *Chandra* and *XMM–Newton* data simultaneously.

T_X 10^6 K	R_0 R_*	f_X 10^{-3}	T_X 10^6 K	R_0 R_*	f_X 10^{-3}
	Model A			Model B	
1.0	4.84	26.93	1.0	4.45	50.67
2.0	4.56	7.22	2.0	4.73	14.70
3.0	3.05	4.76	3.0	2.95	8.31
7.0	2.60	0.34	7.0	2.63	0.72
	Model C			Model D	
1.0	3.89	123.0	1.0	6.10	12.79
2.0	4.72	62.03	2.0	3.40	1.111
3.0	2.77	24.58	3.0	3.85	1.66
7.0	2.89	4.26	7.0	2.14	0.029

The observed fluxes were calculated by fitting Gaussian profiles for each H-like line and He-like triplet. Also, we calculated the fluxes for Fe lines around 15 Å and 17 Å. Each of these blends (two lines around 15 Å and two more around 17 Å) were treated separately, but their fluxes were added in order to compare them with the model values whose fluxes were estimated taking into account the whole blend.

Fig. 13 shows the measured X-ray line fluxes and the ones from model 'A'. There are not strong trends that would suggest changes in abundances. The model line fluxes for N VII Lyα and N VI are too small compared with observations – increasing the nitrogen abundance by 30 per cent would bring them into better agreement.

In order to quantify the consistency of the abundances we calculated line flux ratios that show a low temperature dependence. We used the ratios expressed in equations (4) and (5). The dependence of these flux ratios on temperature is shown in Figs 14(a) and (b) for a grid of models with the same abundances as in model 'A' (solid lines) and in a model with solar abundances from Asplund et al. (2009)(dashed lines). For each set of abundances we also examined the effect of the starting X-ray emission radius (i.e. R_0). The line ratios depend on R_0 due to the strong dependence of the opacity on wavelength. As longer wavelength lines are less attenuated at higher R_0, the N(Hα)/O(Hα+He) ratio will increase with R_0. Also, higher temperatures favour the presence of N VII, while O VIII + O VII is almost constant. This highlights the need for a reliable emission model if abundances are to be derived from X-ray data.

Table 10 shows the values of these ratios for model 'A', the same model but with a nitrogen abundance enhanced by a factor of 1.3 compared with observation (with errors in parentheses). The enhanced nitrogen model improves the agreement between the observed and model values. Such a small correction is within the error

Table 8. '*C*' statistics from fits of H-like (Lyα) and He-like *Chandra* lines. The values in the parentheses are the number of bins used for each line fit.

Ion	Si XIII (35)	Mg XII (22)	Mg XI (50)	Ne X (30)	Ne IX (80)	O VIII (50)	O VII (145)	N VII (66)
σ^a	–	350	–	610	–	706	–	765
C(A)	31.39	17.25	55.93	23.91	67.19	54.36	132.66	79.42
C(B)	31.66	17.81	56.62	24.66	68.22	50.69	131.47	79.22
C(C)	34.75	18.63	58.89	27.15	70.07	48.82	133.50	80.20
C(D)	28.27	15.91	54.76	31.93	78.95	88.40	153.49	78.92

[a]The HWHM (in km s^{-1}) of the Gaussian fit to the line profile.

Table 9. '*C*' statistics from fits of H-like (Lyα) and He-like XMM lines.

Ion	Ne X (20)	Ne IX (68)	O VIII (38)	O VII (88)	N VII (46)	N VI (106)	C VI (45)
σ^a	610	–	706	–	765	–	880
C(A)	18.46	64.61	58.56	109.60	56.51	164.83	69.97
C(B)	18.32	64.11	57.28	107.53	56.52	166.93	69.81
C(C)	18.37	64.10	57.79	104.16	57.47	165.10	71.16
C(D)	19.64	68.66	73.24	126.13	56.61	159.85	71.82

[a]The HWHM for each line in km s^{-1}.

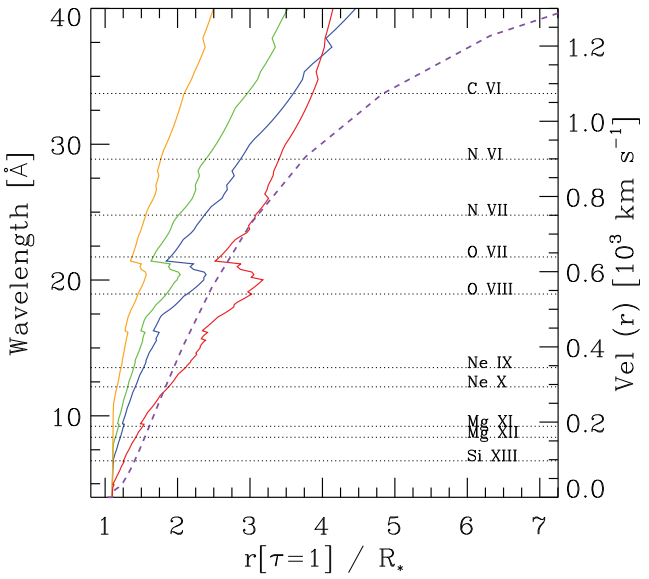

Figure 10. The radius where the continuum optical depth is equal to 1 ($R_{\tau_X=1}$) for wavelengths from 4 to 40 Å. The curves are as follows: model A (blue), B (green), C (orange) and D(red). The dashed purple line shows the velocity profile through the wind while the black dashed lines show the wavelengths for the main H-like and He-like lines. As we lower $\dot{M}$ the radius at which $\tau_X = 1$ is also reduced. The less steep increase of $R_{\tau_X=1}$ for the smooth model at longer wavelengths ($\lambda > 30$ Å) is caused by ionization of He^+ to He^{++} (see Section 6).

estimated for the N abundance determined from optical and UV data. We conclude that the relative abundance values derived from the X-ray analyses are statistically consistent with those derived from UV and optical analyses, and indicate a modest enhancement of N relative to both C and O.

5.6 Interclump medium

Zsargó et al. (2008) pointed out that it is necessary to include the interclump medium radiation in order to reproduce the line strength for O VI in ζ Pup. They showed that when the progenitor of the superion (e.g. N III for N V) is the dominant ion in the wind, the line optical depth does not depend on wind density, and hence the interclump medium, with its larger volume, can contribute significantly to the strength of superion line profiles. We find that this is also the case for ϵ Ori.

Figs 15(a) and (b) show that our clumped model does not reproduce the observed line profiles for N V λ1238, 1242 and O VI λλ1031, 1037(red line) in ϵ Ori. Using the method of Zsargó et al. (2008), we calculated the emission from a tenuous medium between the clumps. This medium occupies most of the wind volume, with a filling factor $f_{ICM} \sim 0.9$–0.95. For this exercise we used the same radiation field from the clumped model – this field is independent of the ICM. We scaled the wind density by two factors, such that $\delta_{ICM} = \alpha \times \delta_{cl}$, where the δ_{cl} is the density in clumps, with $\alpha_1 = 0.1 \times f_\infty$ and $\alpha_2 = 0.05 \times f_\infty$, and assumed that the new component is smooth due to its high filling factor. We calculated this model independently from the clumped model and the hot plasma, but using the same hydrostatic structure.

Figs 15(a) and (b) show the line profiles calculated for two ICM models corresponding to model 'A' with a density contrast between clumped and ICM of $0.1 \times f_\infty = 0.01$ (blue line) and $0.05 \times f_\infty = 0.005$ (green line). These values mean that less than 10 per cent of the wind mass is in the interclump medium. The figures show that the ICM models predict line profiles quite similar to those observed for the N V and O VI lines, while the clumped model (red line) fails to reproduce the profiles. We also tried models with even more tenuous interclump media, but the superion line profiles started to weaken.

Fig. 16 shows the Sobolev optical depth of the N V λ1238 and O VI λ1032 transitions for the clumped model (red), and the ICM models with a density contrast of 100 (blue) and 200 (green). It is evident that there is a large increase in the optical depth in both lines in the ICM models. In their analysis of ζ Pup, Zsargó et al. (2008) found that the flux of the N V line has contributions from the clumps as well as from the ICM. In the case of ϵ Ori, we found that most of the line flux comes from the ICM for both the O VI and N V lines. The importance of the ICM medium for these lines arises because of ionization effects.

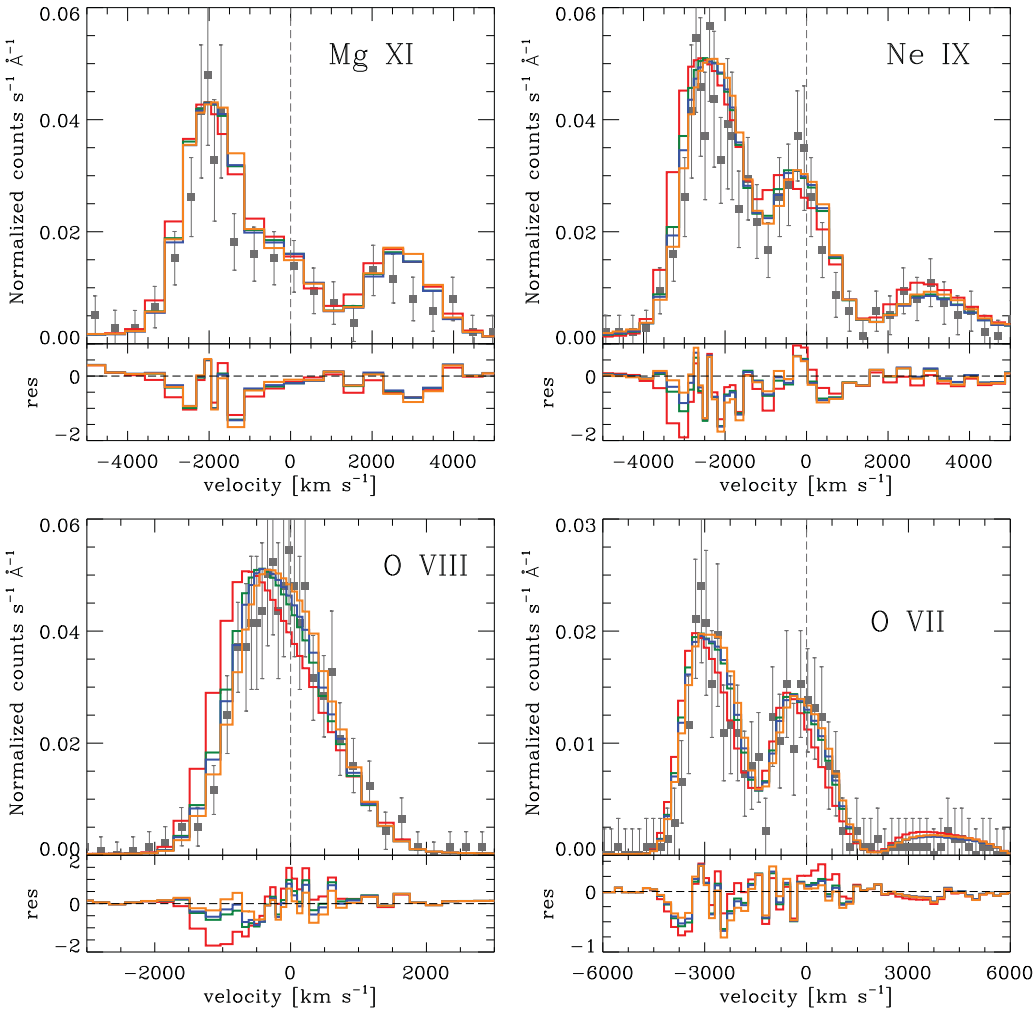

Figure 11. Observed *Chandra* (squares) and synthetic line profiles corresponding to model A (blue), B (green), C (orange) and D (red). Note the primary difference among the models is the notable line asymmetry for the highest $\dot{M}$ model, especially for the longer wavelength lines where wind opacity is higher. Lower panels show the residuals.

The ICM has only a very weak influence on other lines due to its much lower density. The ICM medium is important for the O VI and N V lines because they arise from impurity species whose population is almost independent of density in the wind if they arise from Auger ionization, and if O IV and N III are the dominant ions. Its influence on ρ^2 dependent lines, such as Hα, is insignificant as was already pointed out by Sundqvist et al. (2011), and as confirmed by our own calculations. Sundqvist et al. (2011) note that macro clumping does lead to a slight weakening of Hα.

5.7 Rotation

We chose model 'A' in order to study in more detail the influence of rotation on the spectrum. We re-calculated the spectrum using the two-dimensional method of Busche & Hillier (2005) as described in Section 4, with the same value for the $v\sin i$ = 70 km s^{-1} estimated from the optical data.

Fig. 17 shows the Hα profile calculated using the convolution method (solid blue line) and the two-dimensional radiative transfer method (solid red line). There is a notable difference between the line profiles. The 2D profile shows weaker absorption and emission, as well as a more extended red wing emission. This strong difference, while at first surprising for such a low rotation rate (70 km s^{-1}), can be explained from the high value of β. A high value for this parameter yields a more extended region where the Hα line is produced, and where differential rotation can affect the line profile. The main reason for that difference is the dependence of profile shape on the impact parameter as was pointed out by Hillier et al. (2012). This dependence redistributes the fluxes through the line, yielding wider wings emission and lower flux at the line core for both the absorption and emission components. As a consequence, a weaker P Cyg profile is produced.

In order to reduce the effect described above, we reduced the rotation parameter ($v\sin i$) to 40 km s^{-1} and re-calculated the Hα profile using the 2D code. The resulting profile is shown in Fig. 17 (green line). It is clear that this profile reproduces better the line shape than the former with $v\sin i$ = 70 km s^{-1}. The rest of the optical lines, such as Si III $\lambda\lambda$4453–4576, are well reproduced with 40 km s^{-1}, but with a macroturbulence of ∼90–100 km s^{-1} and $\xi_{\rm min}$ = 15 km s^{-1}. However, such a low rotation had not been reported until recently – Martins et al. (2015) found the same rotation value for ϵ Ori in their variability study of OB stars. Their value is based on the fast Fourier transform method (see Simón-Díaz & Herrero 2007; Gray 2008).

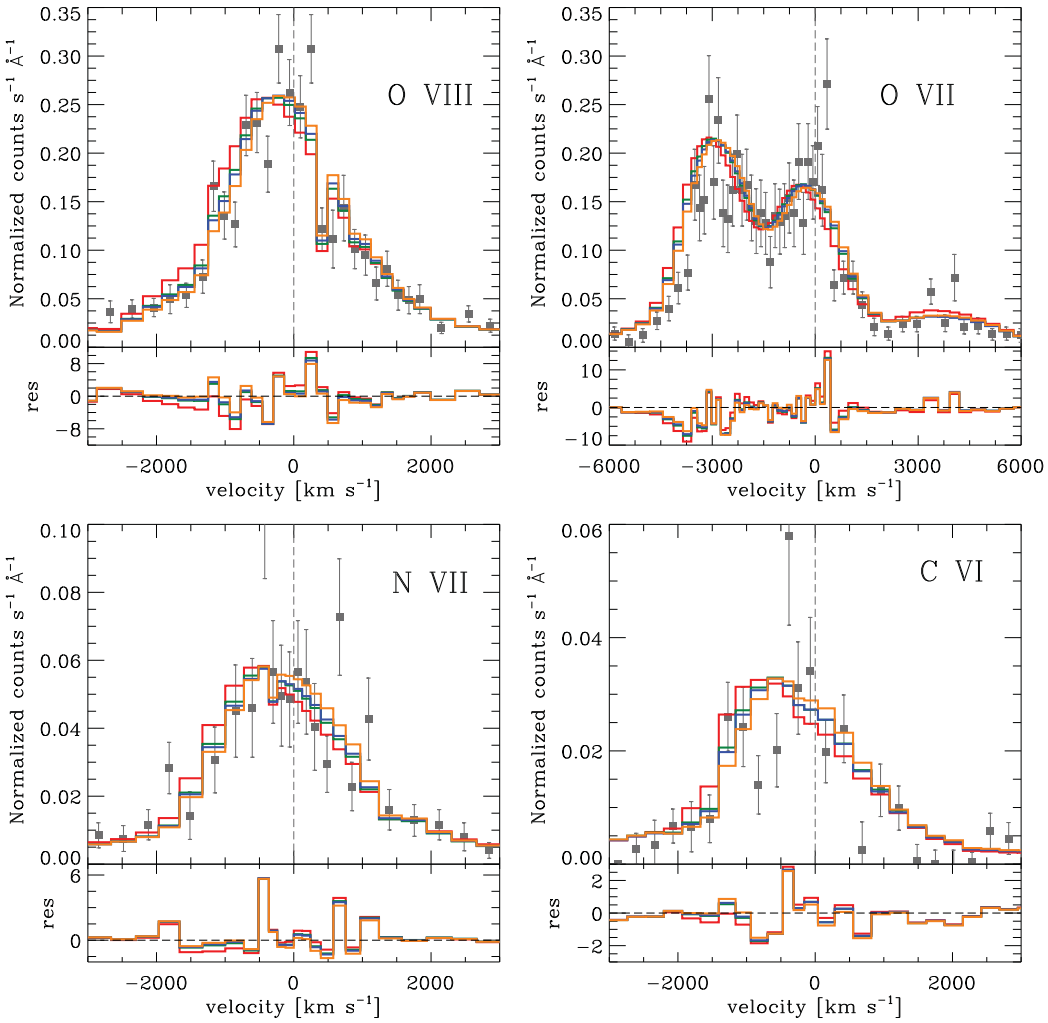

Figure 12. Observed *XMM–Newton* (squares) and synthetic line profiles corresponding to model A (blue), B (green), C (orange) and D (red). Lower panels show the residuals.

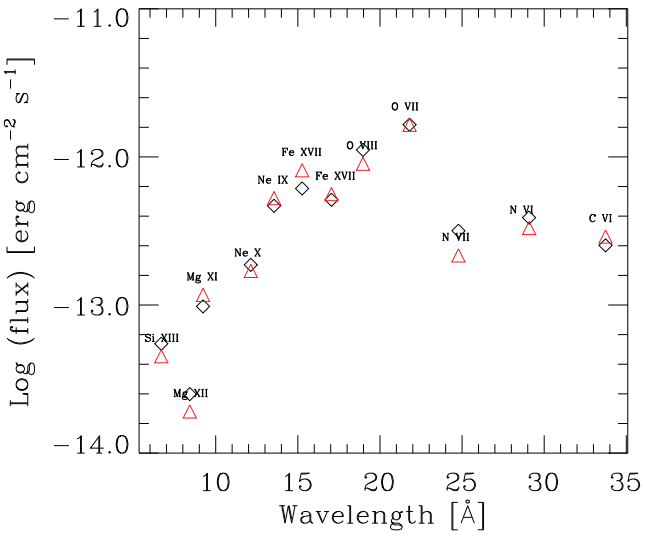

Figure 13. X-ray line fluxes. The observed fluxes are shown as black diamonds while the values for model 'A' are red triangles.

We used the same method to estimate $v \sin i$ based on isolated absorption lines in the optical. The list of lines and the corresponding rotation value are shown in Table 11. All of the $v \sin i$ values are below 70 km s^{-1}, with an average of 43 km s^{-1}, almost identical to the value of 40 km s^{-1} reported by Martins et al.

6 DISCUSSION

In this paper we have presented the results of a multi-wavelength spectroscopic analysis of ϵ Ori. We conclude that the main photospheric and wind parameters computed from optical and UV data are completely compatible with those from an X-ray analysis. We conclude that clumped models with $f_\infty < 0.1$ ($f_\infty \sim 0.1$) are able to reproduce the whole spectrum from the optical to the X-ray band. Nevertheless, there are some points that arose from the analysis that need to be discussed more deeply.

6.1 Hydrodynamical consistency

The high value for β derived here presents some problems for consistency with the momentum wind equation. The radiative force is dominated by momentum transfer in optically thick lines. The

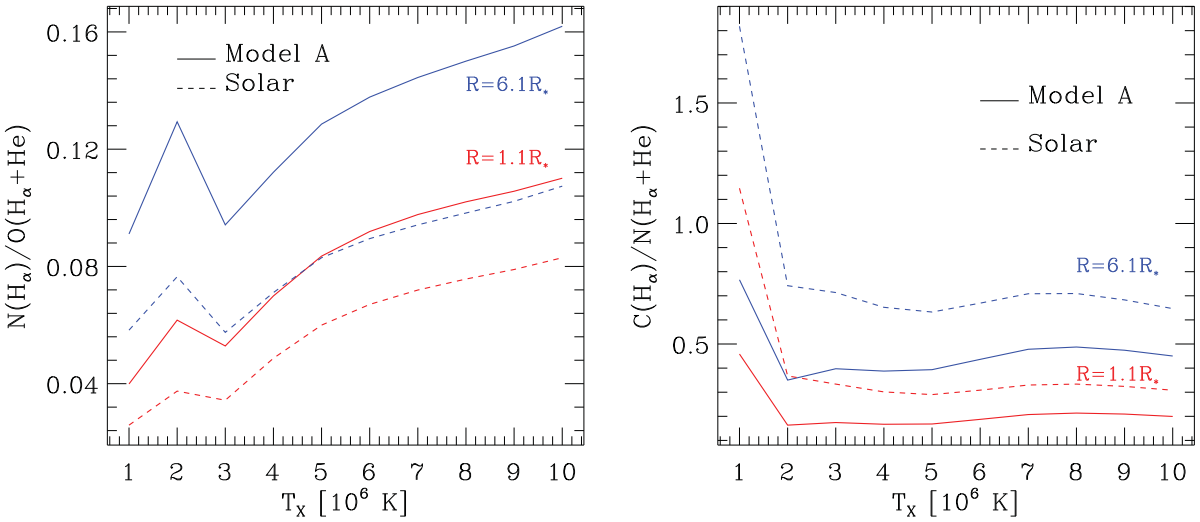

Figure 14. Temperature behaviour of line ratios calculated with equations (4) and (5) with the temperature of emitting plasma (T_X). Blue lines correspond to models in which the X-ray emitting plasma starts at R_0= 6.1 R_* while the red lines correspond to models with R_0 = 1.1 R_*.

Table 10. CNO abundances from X-ray data. Errors on measured values are in parentheses.

	Measured	Model A	Model A 1.3 N	Solar
R(N/O)	0.125 (0.008)	0.10	0.12	0.06
R(C/N)	0.357 (0.020)	0.52	0.39	0.98

strength of this force is proportional to a power of the velocity profile slope (dv/dr), which is steeper when β is low. This means that a high β value will yield lower radiative force that may not be able to drive the wind, especially around the sonic point. Further, a larger value of β implies that the gravity and the radiative force are almost equal.

The momentum equation for a spherically symmetric wind is:

$$v\frac{\mathrm{d}v}{\mathrm{d}r} = -\frac{1}{\rho}\frac{P_\mathrm{g}}{\mathrm{d}r} - g + g_\mathrm{rad}, \quad (6)$$

where P_g is the gas pressure, $g = GM_*/r^2$ and g_rad is the total radiative force. Fig. 18 shows that the right side (red) and the left side (blue) of equation (6) for the model 'A' (left panel) disagree around the sonic point (v_s ∼17 km s^{-1}). This also happens for models B and C. It is easy to see that the radiative force is insufficient to match the velocity profile until approximately 100 km s^{-1}. The discrepancies between the curves are approximately 40 per cent, but around the sonic point they reach 100 per cent. In the outer wind there are also discrepancies but these can probably be overcome by changes in the velocity law. However, given the assumptions of our modelling (simple radial variation of the filling factor, and the neglect of porosity and vorosity), we do not consider this to be a worthwhile exercise.

Some alternatives have been suggested by Bouret et al. (2012) to overcome this problem. One is to increase the mass-loss rate and the filling factor in order to increase the radiative force and to conserve the spectral fitting. But in the case of ϵ Ori, as we described above, a filling factor >0.1 is incompatible with the X-ray and UV spectra. Even the smooth model does not meet the momentum equations around the sonic point.

As discussed by Bouret et al. (2012) and Lucy (2010), one solution to this problem is to reduce the microturbulent velocity in the vicinity of the sonic point (ξ_min) and to decrease the β value. A lower ξ_min will reduce the blocking of continuum radiation coming from the inner atmosphere by the blue line wings, hence boosting the force at the sonic point. A lower β will also increase the line radiative force at the sonic point.

The right panel of Fig. 18 shows the results for a model with the same parameters of model 'A', but with radiative force calculated for $\beta = 1.5$ and $\xi_\mathrm{min} = 5$ km s^{-1}. The mass-loss rate for this model was adjusted to fit the emission strength of Hα. The figure shows that even though the curves approach each other around the sonic point the hydrodynamical equation is still not satisfied.[10] Furthermore, lowering the turbulent velocity contradicts the values derived from the spectral analysis.

Another option is to increase the number of levels taken into account in atomic models as well as to include more species in the computation. To investigate this point we calculated a model increasing the number of levels for Fe ions and including Ne, Cl, Ar, and Ca with solar abundances. However, we found that these changes did not improve the momentum balance for the default wind law with $\beta = 2$ and a microturbulence of 20 km s^{-1}.

The discrepancies may be due to some simplifications that are commonly assumed for modelling stellar winds. Microturbulence and macroturbulence are not well understood, as well as their influence on the wind dynamics, especially around the sonic point. Further, variability of line profiles in ϵ Ori shows that the assumption of a steady-state wind is invalid. Indeed, the difficulty of driving the wind through the sonic point in ϵ Ori may be explicitly linked with the observed variability of Hα.

Recent studies of variability in ϵ Ori have been undertaken by Prinja et al. (2004), Thompson & Morrison (2013) and Martins et al. (2015) based on Hα, Si III and He I line profiles. The detected variability has time-scales of a few days and those works linked wind variability with photospheric activity that could be caused by stellar pulsations or small-scale magnetic fields.

[10] The hydrostatic equation is not exactly satisfied at 10 km s^{-1} in these models as we neglected clumping when the hydrostatic equation was solved. The slight departure of f from unity (e.g. 0.8) in this region is sufficient to cause the observed discrepancy.

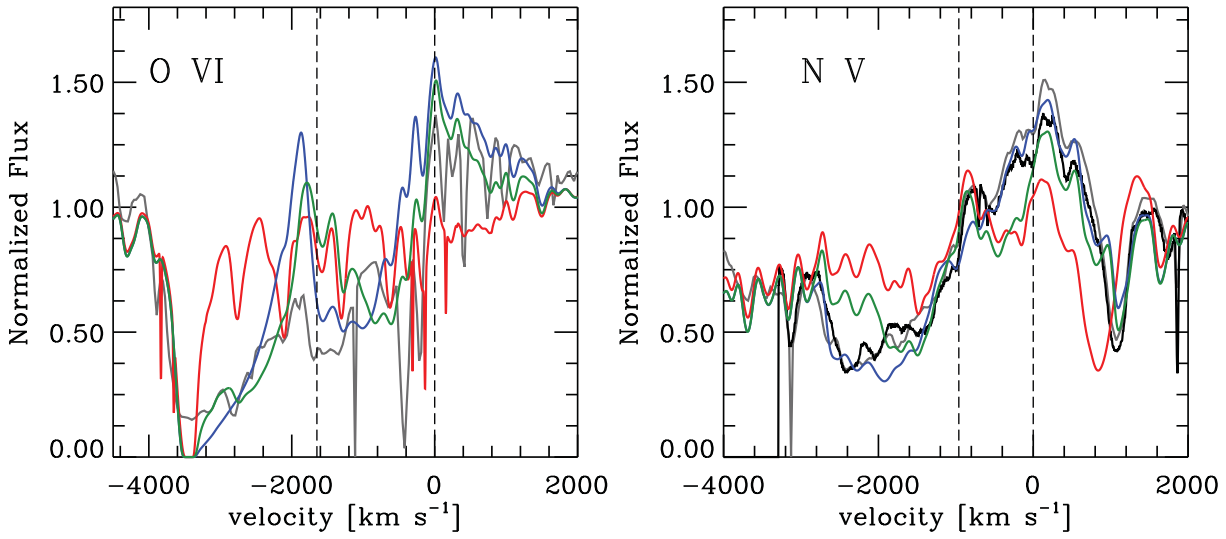

Figure 15. The effect of including the emission of interclump medium. The left panel shows line profiles for O VI λλ1031,1037 and the right panel line profiles for N V λλ1238,1242. The black line corresponds to *GHRS* data, the grey line to *Copernicus* data and the red line to the clumped model 'A'. The blue line corresponds to emission from the ICM with a density contrast of 100, and the green line to a density contrast of 200. A much better fit to the profiles is obtained when we allow for the interclump medium.

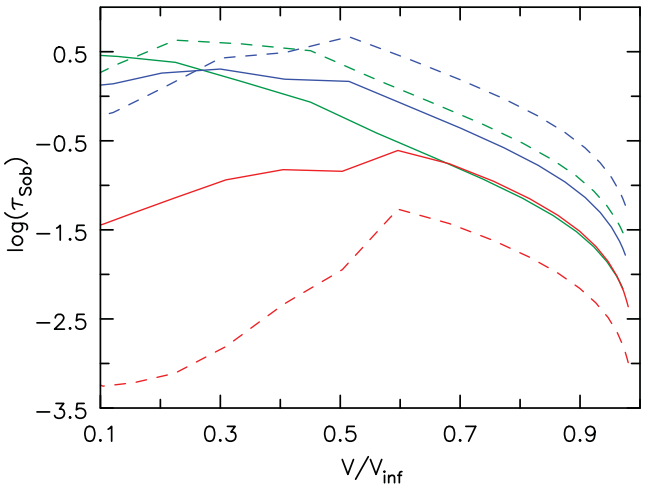

Figure 16. Sobolev line optical depth for N V λ1238 (solid) and O VI λ1032 (dashed). The red lines correspond to the clumped model 'A', while the blue and green lines are for the interclump medium models with density contrasts of 100 and 200, respectively.

6.2 S IV profiles

As for phosphorus, sulphur has a relatively low abundance, and hence its resonance lines commonly appear unsaturated. As a consequence these lines can provide useful constraints on the mass-loss rate, especially if S^{3+} is the dominant ion in the wind (as it is for ϵ Ori). The lower left panel of Fig. 5 shows the dependence on filling factor of the theoretical profiles for the S IV λλ1062,1073 doublet.[11] As is readily apparent from the figure, we are unable to reproduce the observed profile shape even with the lowest f_∞ value (0.01). The sulphur lines show weak absorption and almost no emission in their P Cygni profiles, in stark contrast to the models that show strong emission and blue absorption. Particularly striking is the absence of absorption at high velocities.

As shown in Fig. 19, we can only 'fit' the sulphur doublet if we use an absurdly low abundance (∼0.2 $S_\odot$ with $f_\infty = 0.1$) or filling factor ($f_\infty \sim 0.005$). Even with this abundance, the calculated line profiles show more emission than the data. Moreover, an abundance of 0.2 $S_\odot$ is incompatible with other UV and optical sulphur lines (e.g. S IV λ1098–1100,4486 and S III λ4254). This problem is quite similar to that reported previously with P V λλ1117,1128 in O stars (e.g. Bouret et al. 2003; Hillier 2003; Fullerton, Massa & Prinja 2006, 2008; Bouret et al. 2012), and hence we consider similar solutions.

Various solutions have been proposed for solving the P V λ1117,1128 problem, including the following:

(i) Sub-solar abundance. While factors of 2 variation between stars cannot be ruled out, much larger variations are unlikely. In the present case, other S lines rule this out as the main cause.

(ii) Wrong wind ionization, possibly due to the influence of X-rays. However, the required X-ray flux is higher than observed.

(iii) Wrong wind ionization, possibly because the bulk of the wind has been shocked and not cooled.

(iv) The wind is porous spatially, or porous in velocity space (hereafter called vorosity). Porosity will affect both observed X-ray and UV line profiles, whereas vorosity will only affect UV line profiles.

The influence of X-rays on the ionization structure was analysed by Marcolino et al. (2009) in the context of the weak wind problem of late O dwarf stars. They found that the X-ray luminosity necessary to fit the C IV line strength is approximately 3 dex above the standard value of $L/L_{bol} = -7.0$. In the same sense, Krtička & Kubát (2009, 2012) explored the influence of X-rays on the phosphorus ion fraction $q(P^{+4})$ aiming to fit the P V lines. They concluded that hard X-ray emission does not have a strong effect on $q(P^{+4})$, whereas

[11] The λ1073 line is a blend of two lines at 1072.96 Å ($gf = 0.168$) and 1073.51 Å ($gf = 0.0156$) which have the same lower level. The λ1062 line has a $gf = 0.1$ (Kramida, A., Ralchenko, Yu., Reader, J. and NIST ASD Team 2014. NIST Atomic Spectra Database (version 5.2). Available: http://physics.nist.gov/asd. National Institute of Standards and Technology, Gaithersburg, Md).

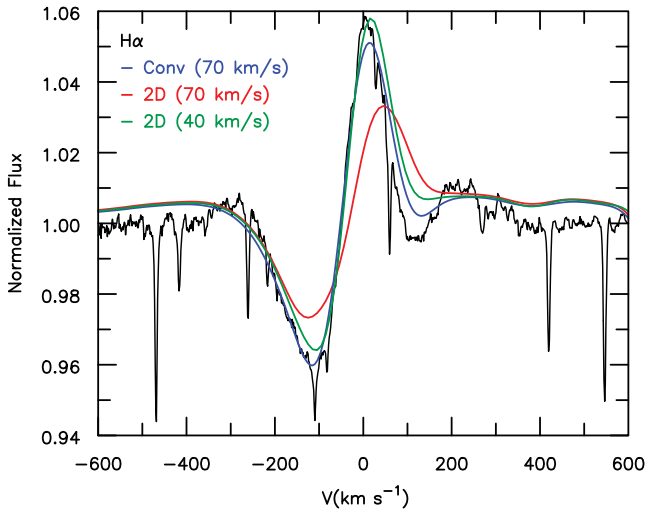

Figure 17. Hα profiles from model 'A'. Rotation is accounted for using different methods: convolution with a 70 km s^{-1} kernel (blue), 2D profile with $v\sin i = 70$ km s^{-1} (red) and 2D profile with $v\sin i = 40$ km s^{-1} (green) (see text for details).

Table 11. Rotation parameter $v\sin i$, calculated using the fast Fourier transform method for the listed optical lines.

Line Ion λ [Å]	$v \sin i$ km s^{-1}
C II 4267	46
N II 3996	33
Si III 4569	39
Si III 4576	39
O II 4592	42
O II 4597	39
O II 4663	56
He I 4389	56
He I 4471	55
He I 4715	38
He I 5017	32

XUV (54–124 ev) emission yields a $q(P^{+4})$ according to observations. However, X-ray and XUV emission affects the ionization structure of other ions (e.g. C VI, N IV and O III). This influences the wind terminal velocity value in a non-negligible way, contradicting the observations (Krtička & Kubát 2012).

In our models, the influence of X-rays on the ionization fraction of S^{+3} is less than 5 per cent for the clumped winds ($f_\infty = 0.01$–0.1), while for the smooth wind the $q(S^{+3})$ is ∼25 per cent. Manipulating the f_X values for the cold plasma (1×10^6 K), we computed a model with an enhanced emission in the range of 160–250 Å, just above the ionization threshold of S IV. We found that even though the bluer absorption component of S IV lines is weakened, it was not enough to fit the observed profiles. Furthermore, the XUV radiation needed to fit the lines would be extremely high. Moreover, we obtained reasonable S IV profiles setting R_0 deeper in the wind ($R_0 = 1.1$ R$_*$). Nevertheless, this change increases the P V abundance in such a way that the lines P V λλ1118,1128 become too strong. Besides that, such R_0 value is ruled out by X-ray analysis.

Macroclumping (porosity) could reproduce the resonance lines of P V without requiring extremely low mass-loss rates, since optically thick clumps will reduce the effective opacity of the lines (e.g. Oskinova et al. 2007; Owocki 2008).

Another effect to be taken into account is the so-called 'velocity–porosity' or *vorosity* (Owocki 2008) that evaluates the effect of a non-monotonic velocity or a velocity field with strong jumps or holes (in the velocity space) on line radiative transfer.

Owocki (2008) showed that *vorosity* yields a reduction in line absorption but it is low (10–20 per cent). This makes the *vorosity* effects weak when compared with *porosity* ones. However, simulation from Sundqvist et al. (2010, 2011) (see also Sundqvist, Puls & Owocki 2014) points out that *vorosity* has an important effect on UV profiles that improves the agreement between optical and UV line mass-loss rates.

Using 3D Monte Carlo simulations, Šurlan et al. (2012, 2013) argue that porosity dominates over vorosity effects. An issue with all of these studies is that they primarily utilize the P V profiles – consequently the fit parameters are not unique.

We postulate that the problem of S IV λλ1063,1073 is analogous to the P V problem, and this gives us a good chance to study clumping in early B stars where P V is not the dominant ion. Furthermore, looking at the *Copernicus* and *FUSE* catalogues of galactic B stars, it is clear that S IV lines are weak even though we expect that it is the dominant ion in the early B stellar winds.

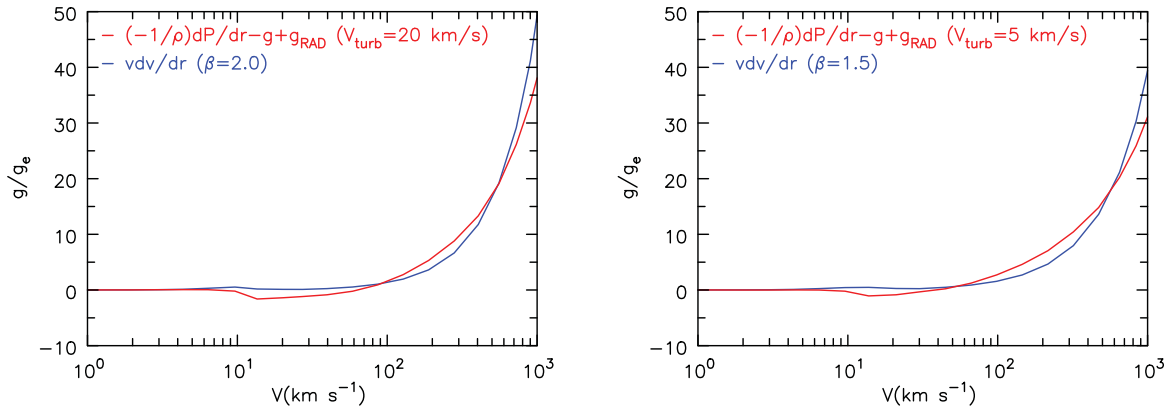

Figure 18. Comparison between velocity profile and acceleration terms from momentum equation (6) divided by the radiative acceleration of free electrons (g_e). Left panel corresponds to model 'A' with acceleration parameter $\beta = 2.0$ and $\xi_{\rm min} = 20$ km s^{-1}. Right panel corresponds to the same model, but with acceleration parameter $\beta = 1.5$ and $\xi_{\rm min} = 5$ km s^{-1}.

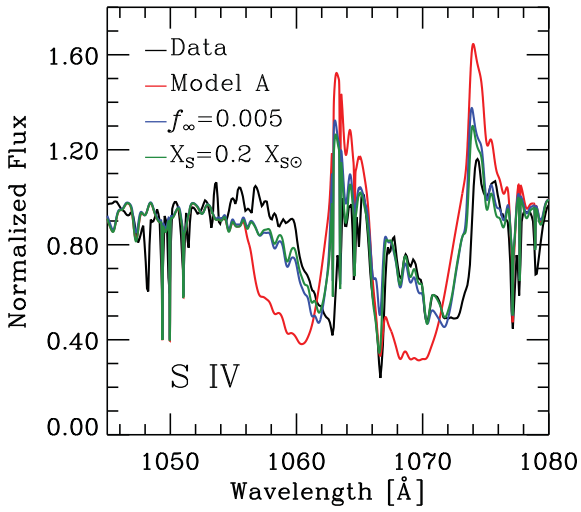

Figure 19. Comparison of the observed line profiles of S IV λλ1062,1073 with synthetic profiles computed using the model 'A' parameters (red), high clumped model (blue) and low sulphur abundance model (green). The black line corresponds to *Copernicus* data.

More evidence for the existence of porosity and vorosity effects can be found in the optical depth ratio of UV resonance doublets. Prinja & Massa (2010) pointed out that this ratio should be equal to the ratio of the oscillator strengths when the clumps are optically thin while for optically thick clumps this ratio is equal to 1. The doublet Si IV λλ1393,1402 is an excellent candidate for this diagnostic since the oscillator strength ratio is ∼2 and the splitting between the components ($\Delta v \sim 1940$ km s^{-1}) is large (although it is less than 3600 km s^{-1}, twice the computed terminal velocity). The data show that the absorption associated with the Si IV doublet components is significantly weaker than the model profiles which are relatively insensitive to the assumed volume filling factor (see second panel from Fig. A5). This could be evidence for a reduction in the effective opacity by porosity and/or vorosity.

In the case of S IV λλ1062,1073, the red component is stronger, with a *gf* value twice that of the blue component. Thus, if vorosity were the dominant effect models that fit the red component (by adjusting the abundance or filling factor) would underestimate the strength of the blue component. Surprisingly, this is not the case – if anything our models do a worse job at matching the bluer component with our models having too much absorption at high velocities. Excluding issues with the observational (and atomic) data, this would suggest that the problem is with the ionization structure of the wind, not an issue with vorosity. Further evidence comes from the shape of the profile. In standard calculations holes in velocity space decrease with velocity, leading to enhanced absorption near the terminal velocity which is not seen in the observed profiles (e.g. Sundqvist et al. 2014). Petrov, Vink & Gräfener (2014) suggested that Hα could be affected by vorosity, but only for stars below the bi-stability jump. ϵ Ori is above that limit; furthermore, Sundqvist et al. (2011) showed that these effects are weak on Hα. Thus Hα does not provide a suitable diagnostic of porosity.

6.3 X-rays

An important aspect of our calculations is the derivation of the spatial distribution of the X-ray emitting plasmas in the wind. The R_0 values from Table 7 are higher than previous estimates for other massive stars (see e.g. Leutenegger et al. 2006) or even with those reported by Cohen et al. (2014a) for ϵ Ori itself. We also found a trend of R_0 versus emitting ion. This trend does not contradict the numerical simulations that predict strong acceleration of some elements of the wind close to the surface (Feldmeier et al. 1997; Runacres & Owocki 2002; Dessart & Owocki 2003, 2005), since it could be caused by optical depth effects.

The main reason for the larger R_0 is the high value of β. With a larger β the wind velocity necessary to fit the line widths occurs at larger radii. For a model with $\beta = 1$, R_0 is closer to the surface, and variation of R_0 with the temperature is weaker. This is consistent with the finding of constant R_0 for ϵ Ori by Cohen et al. (2014a). However, we stress that the link between R_0 and β that we found in this work provides a new challenge for understanding shock formation in the wind and the X-ray emission of massive stars. What does R_0 actually mean and what is behind its relation with wind acceleration? In order to understand the underlying physics

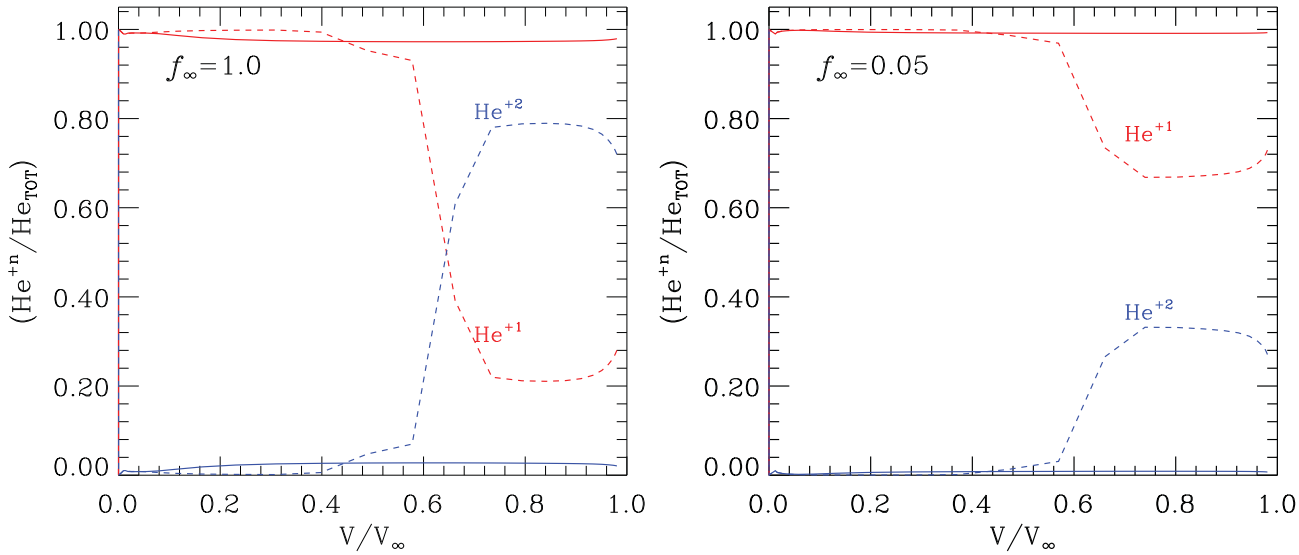

Figure 20. Effect of including X-rays on the ionization structure of He. The solid line corresponds to a model without X-rays, and dashed lines correspond to models that include X-ray emission that fit the *Chandra* and *XMM–Newton* data.

of these connections, it is necessary to expand the analysis to more systems.

From the models, it is possible to estimate the region where the bulk of each component of He-like lines is emitted. The local contribution to line flux is proportional to $r^2 n_p^2(r)\epsilon(r)$, where $\epsilon(r)$ is the line emissivity and n_p is the density of the emitting plasma. For instance, for O VII He α, the intercombination component (i) has its maximum contribution at $\sim$4.6 R_*. For the forbidden component (f), the corresponding value is $\sim$28.5 R_*. These values show that the different components of He-like triplets are mostly produced in different regions in the wind.

One caveat with our analysis is that our assumption of a small set of single-temperature plasmas to describe the shock emissions is not realistic. In the inner wind the cooling time ($T_{cool} \sim 1/\rho$) for each shock is less than the dynamic time, and hence modelling of the shock structure is required to accurately predict the X-ray emission. This will be explored in the future.

All of our models yield asymmetric lines, with a lower degree of skewness for models with lower filling factor. The observed blueshifts of approximately 210 ± 123 km s^{-1} for lines with wavelength $\lambda \gtrsim 10$ Å provide clear evidence of wind absorption. While a clumped wind is necessary to fit the line profiles we cannot distinguish between the 'A' and 'B' models with $f_\infty = 0.1$ and 0.05, respectively. Both models yield adequate X-ray profiles with reasonable mass-loss rates without requiring the inclusion of porosity or resonance scattering effects. This confirms the mass-loss rate derived by Cohen et al. (2014a) that did not use porosity effects to fit X-ray line profiles. Our results and those of Cohen et al. cannot confirm the absence of porosity. Much higher signal-to-noise X-ray observations are needed if tighter constraints are to be obtained. Moreover, due to the strong variability of Hα, the influence of non-spherical winds and temporal variability should be considered.

It is generally assumed that X-rays do not strongly affect the X-ray opacity of the 'cool' wind. In the case of ϵ Ori we found that this is not necessarily true. In ϵ Ori the X-rays can ionize He^+ in the outer wind (Fig. 20), reducing the X-ray opacity (see the behaviour at outer regions of the red line in Fig. 10). The effect is largest in the unclumped model. Normally, X-rays do not strongly affect the dominant ionization stage as X-ray flux is generally small compared with the UV ionizing flux near the relevant thresholds – this is not the case for ϵ Ori.

The effect of X-rays on He ionization in wind has two consequences: (1) for modelling B or later stars, it is important to consistently take into account the interaction of X-rays with the wind in order to estimate the wind parameters, and not separately as commonly done for O stars. (2) The value of the mass-loss rates computed using X-ray line profiles may be biased towards low values if this effect is not taken into account.

Finally, our preferred models, A and B, show a very strong trend of higher X-ray filling factors for low temperature emission components (see Table 7). This model fitting result accounts for both wind absorption and the different emissivities of different plasma temperature components, and thus reflects the instantaneous plasma temperature distribution. These results are broadly consistent with a shock-heating analysis that shows a very strong preference for weaker shocks over stronger shocks, with almost no shock heating above 10^7 K.

7 SUMMARY AND CONCLUSIONS

We have presented a multi-wavelength analysis of the early B-supergiant ϵ Ori. This analysis utilizes a modified version of CMFGEN that allows for the radiative interactions between the X-ray emitting plasma and the cool wind.

We get excellent fits to X-ray, UV and optical data. The derived photospheric parameters for ϵ Ori are quite similar to those previously derived ($T_{eff} = 27\,000 \pm 500$ K and $\log g = 3.0 \pm 0.05$). The observed UV fluxes together with the known m_V yield $E(B-V) = 0.091 \pm 0.01$. Using the last *Hipparcos* distance (606 pc), the ϵ Ori luminosity is $\log(L_*/L\odot)\sim5.93$. This luminosity is the highest reported value for ϵ Ori. Using the former *Hipparcos* distance (412 pc), the ϵ Ori luminosity is $\log(L_*/L\odot) \sim 5.60$.

The metal abundances derived from the different passbands (X-ray, optical and UV) are consistent within errors. We derive [N/O] = 0.15 and [N/C] = 0.33 for ϵ Ori. Optically derived CNO abundances show a factor of 2 dispersion about the mean, suggesting there are still some inadequacies in the atomic models, and/or the treatment of turbulence.

The UV S IV λλ1068,1073 profiles show the same problem as reported for P V λλ1117,1128 in O stars (e.g. Fullerton et al. 2006). To fit this doublet (actually three lines but two are blended) it is necessary to use an extremely clumped wind and/or a very low sulphur abundance. The latter is incompatible with other UV and optical sulphur lines. Close examination of the profiles suggests an issue with the calculated ionization structure of the outer wind (possibly related to the presence of a hot plasma), although porosity and vorosity effects may also be important.

A clumped wind, with a volume filling factor of the order of 0.1 or less, produces X-ray profiles consistent with observation, favouring $\dot{M} \leq 4.9 \times 10^{-7}$ $M_\odot$ yr^{-1}, a value approximately four times lower than the one theoretically predicted by Vink, de Koter & Lamers (2000, 2001). However the signal-to-noise ratio of the X-ray data does not allow us to determine an accurate f_X value, or to examine the effects of porosity. We also found evidence that the UV profiles Si IV and S IV could be affected by porosity or problems with the ionization structure.

As found for ζ Pup (Zsargó et al. 2008), we found evidence of resonance scattering from the interclump medium – the traditional clumped model cannot reproduce the observed O VI and N V resonance profiles.

The $\beta = 2$ value reported in this work is higher than found in earlier work, and than that expected from standard wind theory. However the observed Hα is variable, and thus time variable and non-spherically symmetric models are needed to analyse the profiles.

ACKNOWLEDGEMENTS

Support for this work was provided by the National Aeronautics and Space Administration through Chandra Award Number ARO-11002A issued by the Chandra X-ray Observatory Center, which is operated by the Smithsonian Astrophysical Observatory for and on behalf of the National Aeronautics and Space Administration under contract NAS8-03060. This work was also supported by NASA Chandra grants: AR2-13001A and AR0-11002B. D. John Hillier also acknowledges partial support from STScI theory grant HST-AR-12640.01. MAL also acknowledges the support from Chandra, grants: G02-13002A and AR2-130001B. David Cohen also acknowledges the support from Chandra, grants: TM3-14001B, AR0-11002B and AR2-13001A. We also acknowledge Francisco Najarro for his highly valuable comments and suggestions on this manuscript. We are also grateful to Randall Smith for providing us the source code of APEC and to the Chandra X-ray Center for the use of ATOMDB. JZ acknowledges CONACyT grant CB-2011-01

No. 168632. We also thank the anonymous referee for the valuable comments that helped us to improve this manuscript.

REFERENCES

Arnaud K. A., 1996, in Jacoby G. H., Barnes J., eds, ASP Conf. Ser. Vol. 101, Astronomical Data Analysis Software and Systems V. Astron. Soc. Pac., San Francisco, p. 17
Asplund M., Grevesse N., Sauval A. J., Scott P., 2009, ARA&A, 47, 481
Auer L. H., Mihalas D., 1972, ApJS, 24, 193
Bagnulo S., Landolfi M., Landstreet J. D., Landi Degl'Innocenti E., Fossati L., Sterzik M., 2009, PASP, 121, 993
Blomme R., Prinja R. K., Runacres M. C., Colley S., 2002, A&A, 382, 921
Bouret J.-C., Lanz T., Hillier D. J., Heap S. R., Hubeny I., Lennon D. J., Smith L. J., Evans C. J., 2003, ApJ, 595, 1182
Bouret J.-C., Lanz T., Hillier D. J., 2005, A&A, 438, 301
Bouret J.-C., Hillier D. J., Lanz T., Fullerton A. W., 2012, A&A, 544, A67
Bouret J.-C., Lanz T., Martins F., Marcolino W. L. F., Hillier D. J., Depagne E., Hubeny I., 2013, A&A, 555, A1
Brown A. G. A., de Geus E. J., de Zeeuw P. T., 1994, A&A, 289, 101
Busche J. R., Hillier D. J., 2005, AJ, 129, 454
Cash W., 1979, ApJ, 228, 939
Cassinelli J. P., Olson G. L., 1979, ApJ, 229, 304
Chiosi C., Maeder A., 1986, ARA&A, 24, 329
Cohen D. H., Leutenegger M. A., Wollman E. E., Zsargó J., Hillier D. J., Townsend R. H. D., Owocki S. P., 2010, MNRAS, 405, 2391
Cohen D. H., Gagné M., Leutenegger M. A., MacArthur J. P., Wollman E. E., Sundqvist J. O., Fullerton A. W., Owocki S. P., 2011, MNRAS, 415, 3354
Cohen D. H., Wollman E. E., Leutenegger M. A., Sundqvist J. O., Fullerton A. W., Zsargó J., Owocki S. P., 2014a, MNRAS, 439, 908
Cohen D. H., Li Z., Gayley K. G., Owocki S. P., Sundqvist J. O., Petit V., Leutenegger M. A., 2014b, MNRAS, 444, 3729
Crowther P. A., Hillier D. J., Evans C. J., Fullerton A. W., De Marco O., Willis A. J., 2002, ApJ, 579, 774
Crowther P. A., Lennon D. J., Walborn N. R., 2006, A&A, 446, 279
Cunha K., Hubeny I., Lanz T., 2006, ApJ, 647, L143
Dessart L., Owocki S. P., 2003, A&A, 406, L1
Dessart L., Owocki S. P., 2005, A&A, 437, 657
Diplas A., Savage B. D., 1994, ApJS, 93, 211
Drake J. J., Testa P., 2005, Nature, 436, 525
Ebbets D., 1982, ApJS, 48, 399
Evans D. S., 1967, in Batten A. H., Heard J. F., eds, IAU Symp. Vol. 30, Determination of Radial Velocities and their Applications. Academic Press Inc., p. 57
Evans C. J., Crowther P. A., Fullerton A. W., Hillier D. J., 2004, ApJ, 610, 1021
Eversberg T., Lépine S., Moffat A. F. J., 1998, ApJ, 494, 799
Feldmeier A., Puls J., Pauldrach A. W. A., 1997, A&A, 322, 878
Foster A. R., Ji L., Smith R. K., Brickhouse N. S., 2012, ApJ, 756, 128
Fullerton A. W., Gies D. R., Bolton C. T., 1996, ApJS, 103, 475
Fullerton A. W., Massa D. L., Prinja R. K., 2006, ApJ, 637, 1025
Fullerton A. W., Massa D. L., Prinja R. K., 2008, in Hamann W.-R., Feldmeier A., Oskinova L. M., eds, Clumping in Hot-Star Winds. Potsdam University Press, p. 23
Gabriel A. H., Jordan C., 1969, MNRAS, 145, 241
Gray D. F., 2008, The Observation and Analysis of Stellar Photospheres. Cambridge University Press, Cambridge
Harnden Jr, F. R. et al., 1979, ApJ, 234, L51
Hearn A. G., 1975, A&A, 40, 355
Hervé A., Rauw G., Nazé Y., 2013, A&A, 551, A83
Hillier D. J., 1991, A&A, 247, 455
Hillier D. J., 2003, in Hubeny I., Mihalas D., Werner K., eds, ASP Conf. Ser. Vol. 288, Stellar Atmosphere Modelling. Astron. Soc. Pac., San Francisco, p. 199
Hillier D. J., Miller D. L., 1998, ApJ, 496, 407
Hillier D. J., Miller D. L., 1999, ApJ, 519, 354
Hillier D. J., Bouret J.-C., Lanz T., Busche J. R., 2012, MNRAS, 426, 1043
Howarth I., Lamers H. J. G., 1999, J. British Astron. Assoc., 109, 347
Howarth I. D., Siebert K. W., Hussain G. A. J., Prinja R. K., 1997, MNRAS, 284, 265
Ignace R., Gayley K. G., 2002, ApJ, 568, 954
Kaper L., Henrichs H. F., Nichols J. S., Snoek L. C., Volten H., Zwarthoed G. A. A., 1996, A&AS, 116, 257
Knobel E. B., 1909, The Observatory, 32, 357
Krtička J., Kubát J., 2009, MNRAS, 394, 2065
Krtička J., Kubát J., 2012, MNRAS, 427, 84
Kudritzki R. P., Puls J., Lennon D. J., Venn K. A., Reetz J., Najarro F., McCarthy J. K., Herrero A., 1999, A&A, 350, 970
Lamers H. J. G. L. M., 1974, A&A, 37, 237
Lamers H. J. G. L. M., Leitherer C., 1993, ApJ, 412, 771
Lee T. A., 1968, ApJ, 152, 913
Lesh J. R., 1968, ApJS, 17, 371
Leutenegger M. A., Paerels F. B. S., Kahn S. M., Cohen D. H., 2006, ApJ, 650, 1096
Leutenegger M. A., Owocki S. P., Kahn S. M., Paerels F. B. S., 2007, ApJ, 659, 642
Leutenegger M. A., Cohen D. H., Zsargó J., Martell E. M., MacArthur J. P., Owocki S. P., Gagné M., Hillier D. J., 2010, ApJ, 719, 1767
Leutenegger M. A., Cohen D. H., Sundqvist J. O., Owocki S. P., 2013, ApJ, 770, 80
Lucy L. B., 1982, ApJ, 255, 286
Lucy L. B., 2010, A&A, 524, A41
Lucy L. B., White R. L., 1980, ApJ, 241, 300
McErlean N. D., Lennon D. J., Dufton P. L., 1998, A&A, 329, 613
McErlean N. D., Lennon D. J., Dufton P. L., 1999, A&A, 349, 553
Macfarlane J. J., Cassinelli J. P., Welsh B. Y., Vedder P. W., Vallerga J. V., Waldron W. L., 1991, ApJ, 380, 564
Macfarlane J. J., Cohen D. H., Wang P., 1994, ApJ, 437, 351
Maeder A., Meynet G., 2000, ARA&A, 38, 143
Marcolino W. L. F., Bouret J.-C., Martins F., Hillier D. J., Lanz T., Escolano C., 2009, A&A, 498, 837
Martins F., Hillier D. J., 2012, A&A, 545, A95
Martins F., Schaerer D., Hillier D. J., Meynadier F., Heydari-Malayeri M., Walborn N. R., 2005, A&A, 441, 735
Martins F., Marcolino W., Hillier D. J., Donati J.-F., Bouret J.-C., 2015, A&A, 574, A142
Morel T., Marchenko S. V., Pati A. K., Kuppuswamy K., Carini M. T., Wood E., Zimmerman R., 2004, MNRAS, 351, 552
Najarro F., Hillier D. J., Puls J., Lanz T., Martins F., 2006, A&A, 456, 659
Najarro F., Hanson M. M., Puls J., 2011, A&A, 535, A32
Nieva M. F., Przybilla N., 2006, ApJ, 639, L39
Oskinova L. M., Feldmeier A., Hamann W.-R., 2006, MNRAS, 372, 313
Oskinova L. M., Hamann W.-R., Feldmeier A., 2007, A&A, 476, 1331
Oskinova L., Hamann W.-R., Ignace R., Feldmeier A., 2011, Bulletin de la Societe Royale des Sciences de Liege, 80, 54
Owocki S. P., 2008, in Hamann W.-R., Feldmeier A., Oskinova L. M., eds, Clumping in Hot-Star Winds. Potsdam University Press, p. 121
Owocki S. P., Cohen D. H., 2001, ApJ, 559, 1108
Owocki S. P., Cohen D. H., 2006, ApJ, 648, 565
Owocki S. P., Castor J. I., Rybicki G. B., 1988, ApJ, 335, 914
Perryman M. A. C. et al., 1997, A&A, 323, L49
Petit P., Louge T., Théado S., Paletou F., Manset N., Morin J., Marsden S. C., Jeffers S. V., 2014, PASP, 126, 469
Petrov B., Vink J. S., Gräfener G., 2014, A&A, 565, A62
Porquet D., Mewe R., Dubau J., Raassen A. J. J., Kaastra J. S., 2001, A&A, 376, 1113
Prinja R. K., Massa D. L., 2010, A&A, 521, L55
Prinja R. K., Massa D., Fullerton A. W., 2002, A&A, 388, 587
Prinja R. K., Rivinius T., Stahl O., Kaufer A., Foing B. H., Cami J., Orlando S., 2004, A&A, 418, 727
Prinja R. K., Markova N., Scuderi S., Markov H., 2006, A&A, 457, 987
Puls J., Urbaneja M. A., Venero R., Repolust T., Springmann U., Jokuthy A., Mokiem M. R., 2005, A&A, 435, 669

Puls J., Markova N., Scuderi S., Stanghellini C., Taranova O. G., Burnley A. W., Howarth I. D., 2006, A&A, 454, 625
Repolust T., Puls J., Hanson M. M., Kudritzki R.-P., Mokiem M. R., 2005, A&A, 440, 261
Rivero González J. G., Puls J., Najarro F., 2011, A&A, 536, A58
Rivero González J. G., Puls J., Najarro F., Brott I., 2012a, A&A, 537, A79
Rivero González J. G., Puls J., Massey P., Najarro F., 2012b, A&A, 543, A95
Runacres M. C., Owocki S. P., 2002, A&A, 381, 1015
Santolaya-Rey A. E., Puls J., Herrero A., 1997, A&A, 323, 488
Savage B. D., Bohlin R. C., Drake J. F., Budich W., 1977, ApJ, 216, 291
Searle S. C., Prinja R. K., Massa D., Ryans R., 2008, A&A, 481, 777
Seward F. D., Forman W. R., Giacconi R., Griffiths R. E., Harnden F. R., Jr, Jones C., Pye J. P., 1979, ApJ, 234, L55
Silvester J., Wade G. A., Kochukhov O., Bagnulo S., Folsom C. P., Hanes D., 2012, MNRAS, 426, 1003
Simón-Díaz S., Herrero A., 2007, A&A, 468, 1063
Smith R. K., Brickhouse N. S., Liedahl D. A., Raymond J. C., 2001, ApJ, 556, L91
Snow T. P., Jr, Morton D. C., 1976, ApJS, 32, 429
Sundqvist J. O., Puls J., Feldmeier A., 2010, A&A, 510, A11
Sundqvist J. O., Puls J., Feldmeier A., Owocki S. P., 2011, A&A, 528, A64
Sundqvist J. O., Owocki S. P., Cohen D. H., Leutenegger M. A., Townsend R. H. D., 2012, MNRAS, 420, 1553
Sundqvist J. O., Puls J., Owocki S. P., 2014, A&A, 568, A59
Šurlan B., Hamann W.-R., Kubát J., Oskinova L. M., Feldmeier A., 2012, A&A, 541, A37
Šurlan B., Hamann W.-R., Aret A., Kubát J., Oskinova L. M., Torres A. F., 2013, A&A, 559, A130
Thompson G. B., Morrison N. D., 2013, AJ, 145, 95
Trundle C., Lennon D. J., 2005, A&A, 434, 677
Trundle C., Lennon D. J., Puls J., Dufton P. L., 2004, A&A, 417, 217
Urbaneja M., 2004, PhD thesis, University of La Laguna
van Leeuwen F., 2007, A&A, 474, 653
Verner D. A., Yakovlev D. G., 1995, A&AS, 109, 125
Vink J. S., de Koter A., Lamers H. J. G. L. M., 2000, A&A, 362, 295
Vink J. S., de Koter A., Lamers H. J. G. L. M., 2001, A&A, 369, 574
Walborn N. R., 1976, ApJ, 205, 419
Waldron W. L., Cassinelli J. P., 2007, ApJ, 668, 456
Zsargó J., Hillier D. J., Bouret J.-C., Lanz T., Leutenegger M. A., Cohen D. H., 2008, ApJ, 685, L149

APPENDIX A

In this Appendix we present the best-fitting model for each filling factor used in this work $f_\infty = 1.0$ (red), 0.1 (blue), 0.05 (green) and 0.01 (orange). Figs A1 to A3 show the data (black) and the models in the optical band. Fig. A4 shows the *Copernicus* data (black) and the models in FUV. Fig. A5 shows the *IUE* data (black) and the models in UV. The shown models have a rotation $v \sin i = 70$ km s^{-1}and $v_{\rm macro} = 70$ km s^{-1}.

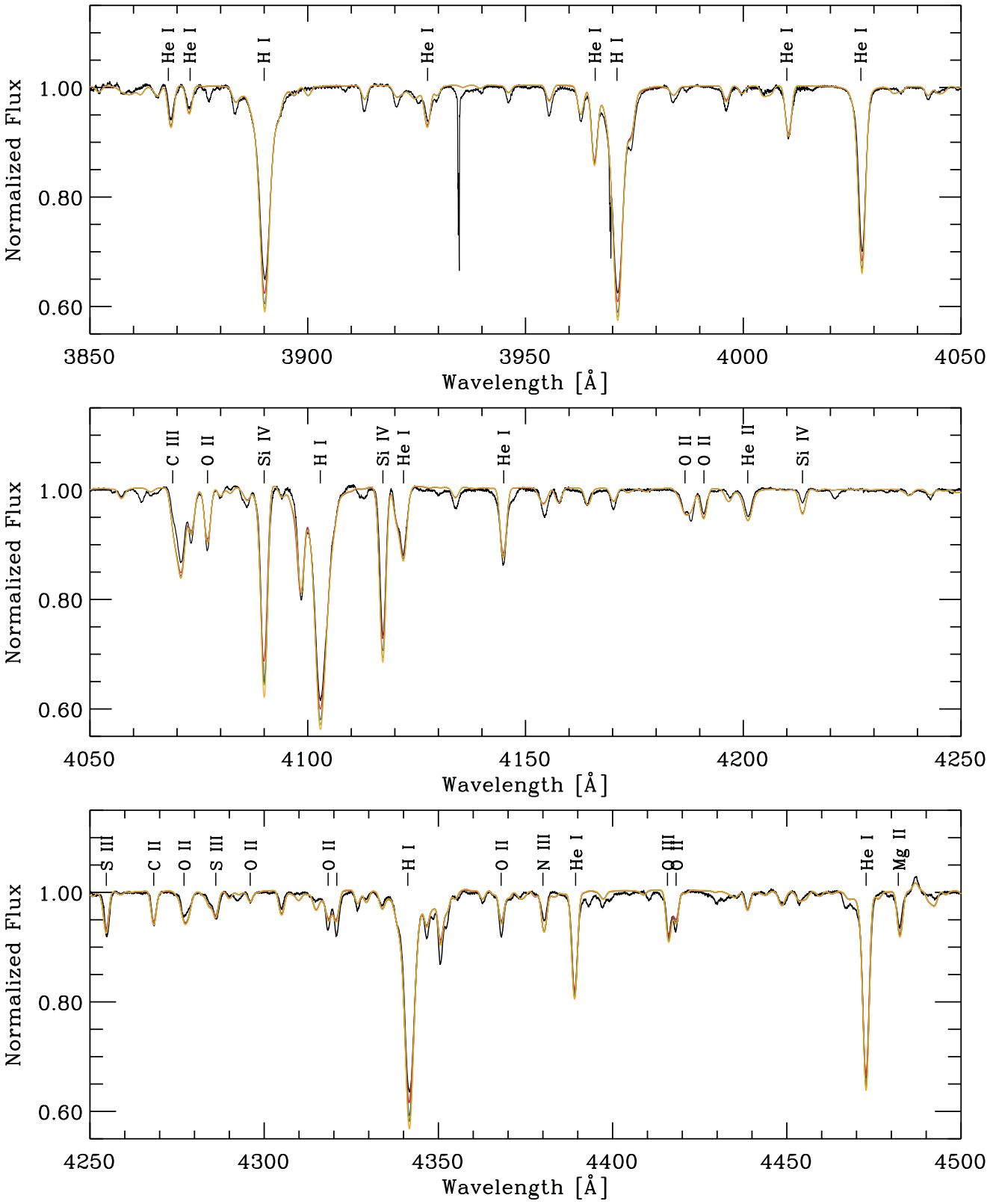

Figure A1. Best model fits for ϵ Ori for each f_∞ value: 1.0 (red), 0.1 (blue), 0.05 (green) and 0.01 (orange). Optical data are shown by the black line.

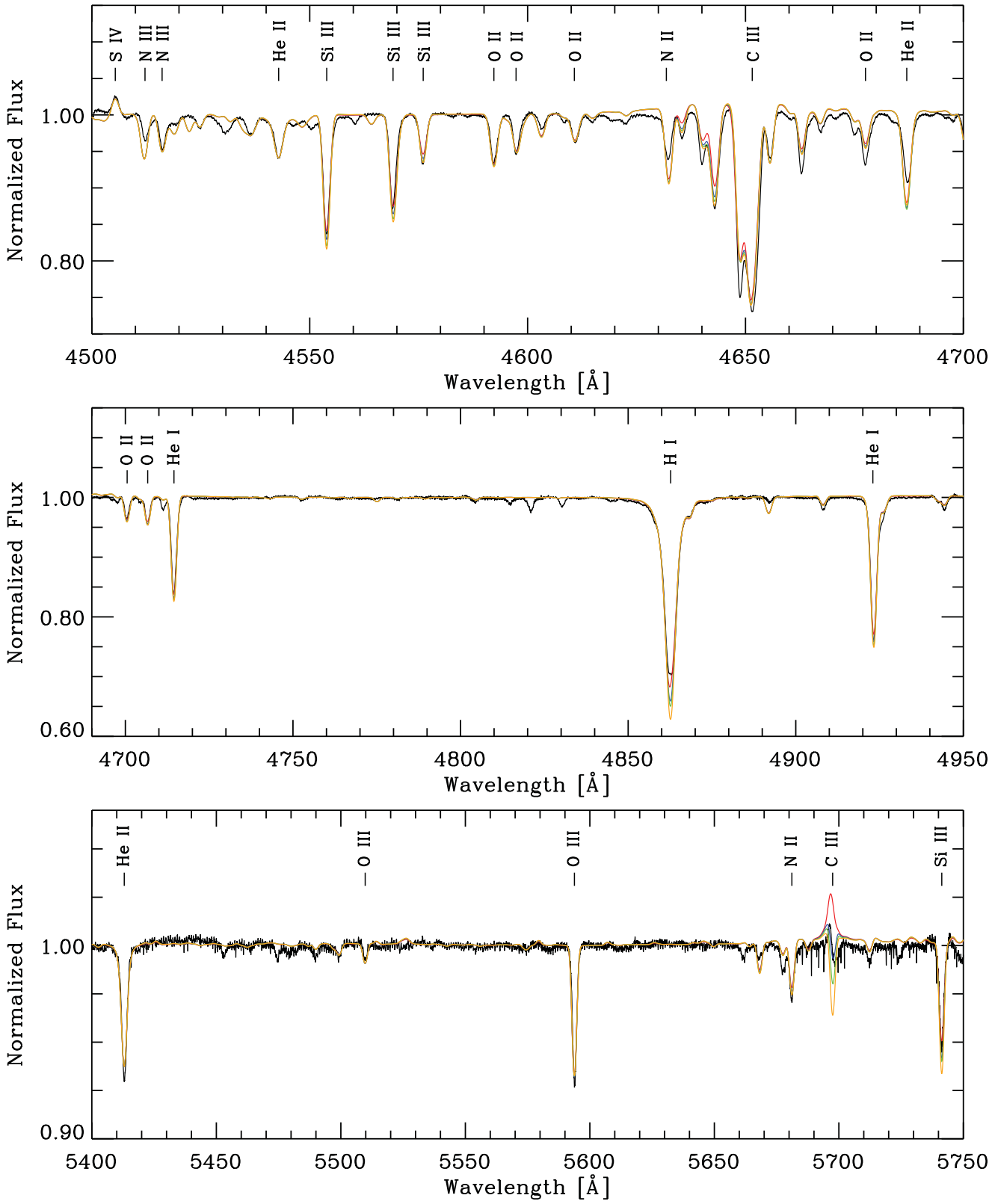

Figure A2. Best model fits for ϵ Ori for each f_∞ value: 1.0 (red), 0.1 (blue), 0.05 (green) and 0.01 (orange). Optical data are shown by the black line.

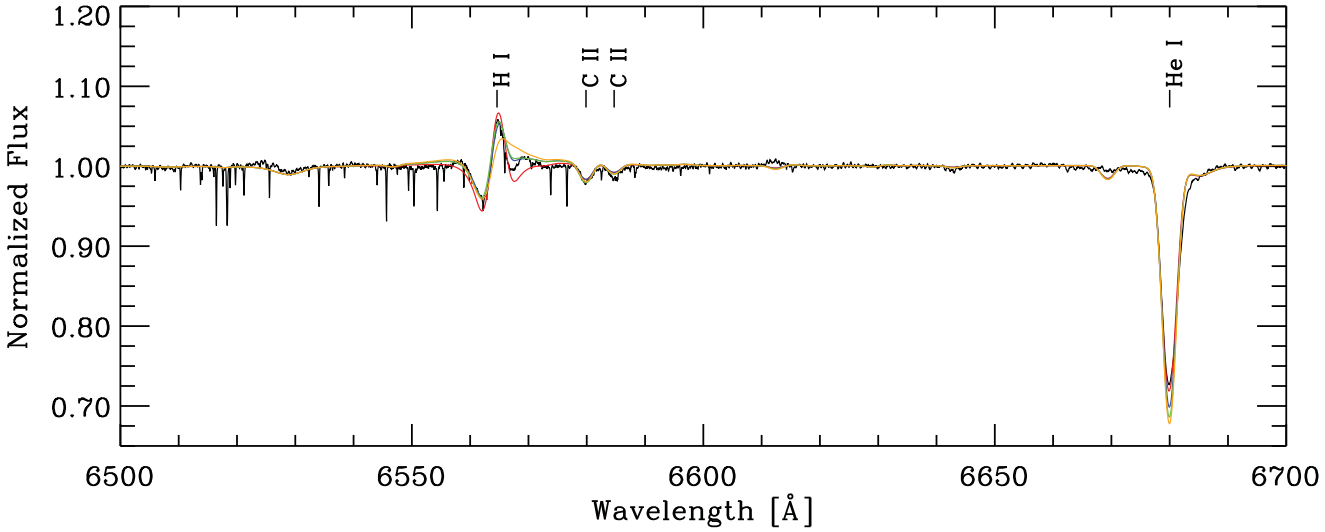

Figure A3. Best model fits for ϵ Ori for each f_∞ value: 1.0 (red), 0.1 (blue), 0.05 (green) and 0.01 (orange). Optical data are shown by the black line.

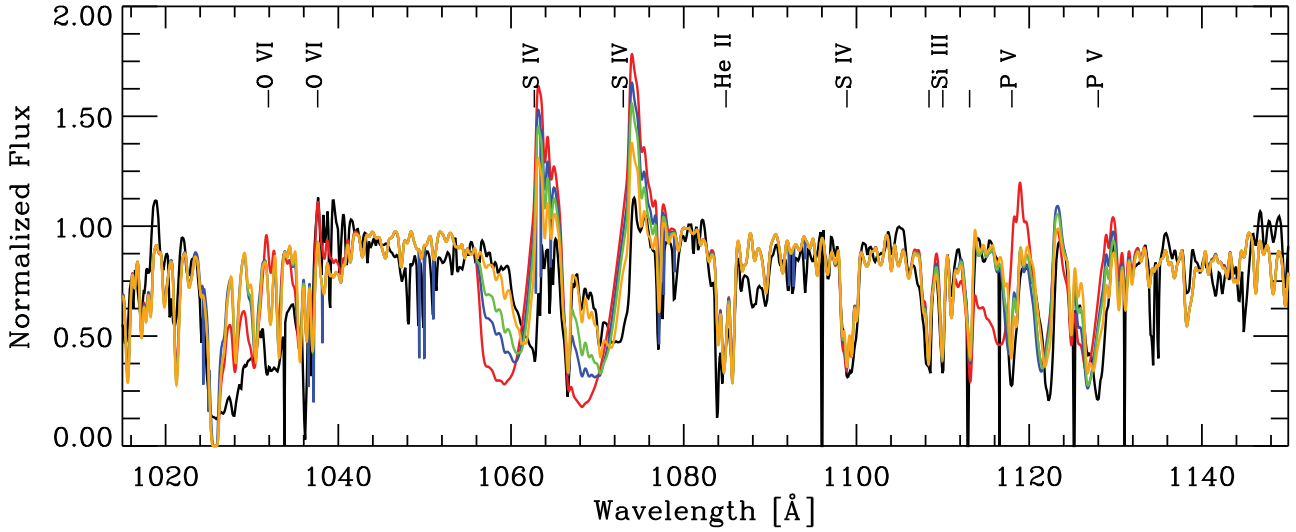

Figure A4. Best model fits for ϵ Ori for each f_∞ value: 1.0 (red), 0.1 (blue), 0.05 (green) and 0.01 (orange). The black line represents the *Copernicus* data. The influence of the interclump medium on O VI λλ1032,1038 has not been included.

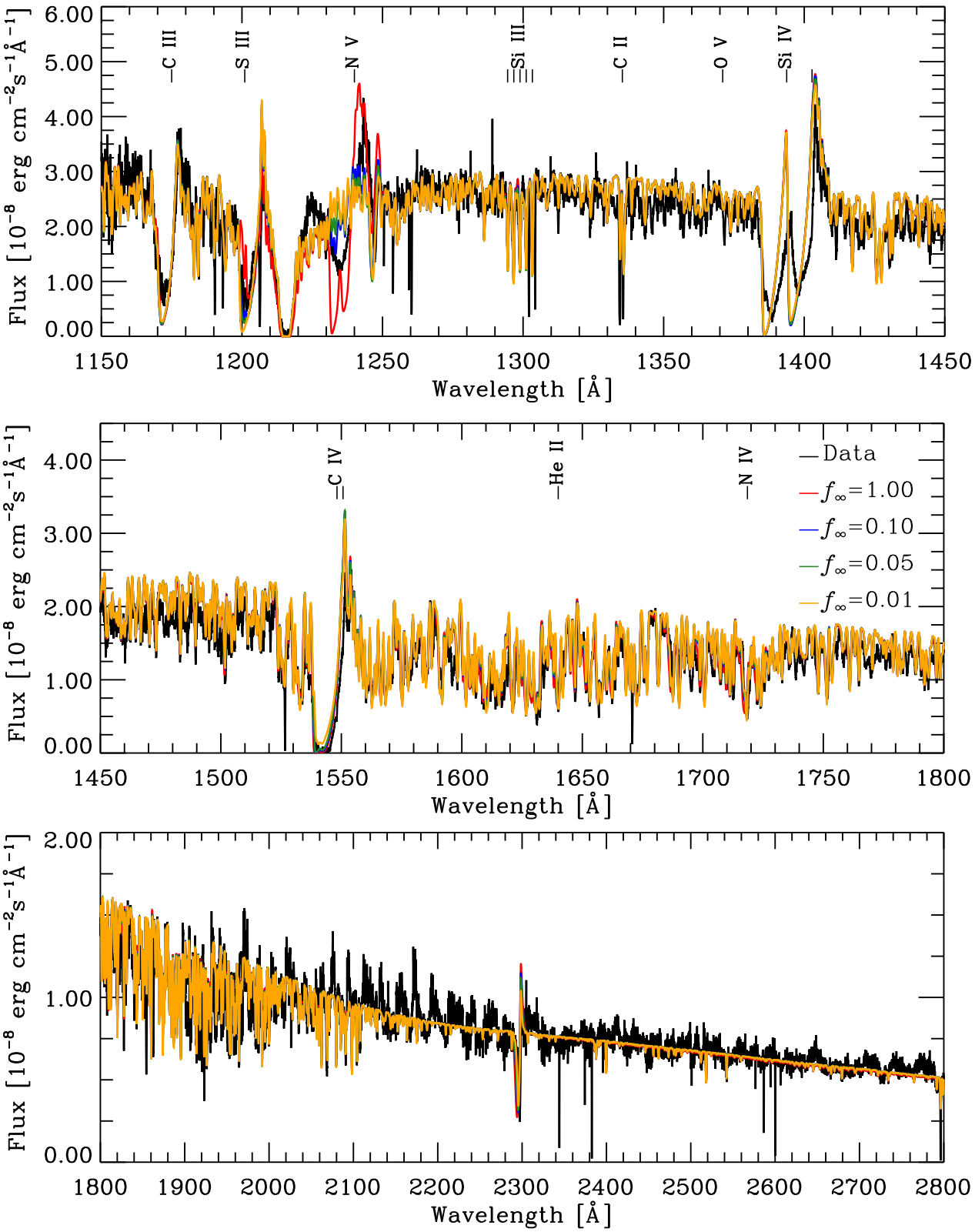

Figure A5. Best model fits for ϵ Ori for each f_∞ value: 1.0 (red), 0.1 (blue), 0.05 (green) and 0.01 (orange). The black line represents the *IUE* data. The influence of the interclump medium on N v λλ1238,1242 has not been included.

This paper has been typeset from a TEX/LATEX file prepared by the author.